Cell Reports
Physical Science

CellPress
OPEN ACCESS

Review

Engineering metal selenides for sodium- and potassium-ion batteries

Yi Lu,[1,2] Ajay Piriya Vijaya Kumar Saroja,[1,2] Runzhe Wei,[1] and Yang Xu[1,*]

SUMMARY

Battery technologies based on Earth's abundant elements are indispensable for sustainable energy storage. Sodium- and potassium-ion batteries (NIBs and KIBs) have begun to show promise as alternatives for lithium-ion batteries. Alongside the discovery of new anode materials, the last few years have seen rapidly increasing interest in metal selenides for NIBs and KIBs. This review presents a timely summary of the recent progress on using metal selenides to electrochemically store Na^+ and K^+. The review features the design strategies for metal selenides and discusses the roles of the strategies in addressing the current issues of applying metal selenides in NIBs and KIBs. Future opportunities are also presented to signpost open questions that are worth investigating to allow further development of metal selenides and their NIB and KIB performance. This review may shed some light on the material design for not only the electrochemical community but also wider research domains.

INTRODUCTION

The exploration of renewable energy resources is crucial due to concerns surrounding environmental pollution and energy demand, and this creates the need for sustainable energy storage technologies, for which batteries hold the key. The successful commercialization of lithium-ion batteries (LIBs), built on their high energy density and durability, has made them the dominating battery technology in the sector of portable electronic devices, and they are being highly pursued in the sector of electric vehicles. However, the lithium and cobalt used in the cathodes for LIBs are unevenly distributed in Earth's crust, which leads to limited availability and potential supply risk, as well as inevitably causing cost rise. The growth and impending demand for LIBs for electric vehicles further raise serious concerns about the availability of lithium resources (0.0017 wt % in Earth's crust) (Figure 1A) in the long run.[1] In this regard, developing sustainable battery technologies based on naturally abundant resources can provide a reliable solution for the existing high demand for energy storage. Sodium-ion batteries (NIBs)[2–4] and potassium-ion batteries (KIBs)[5–7] are suitable substitutes for LIBs because of abundant Na and K resources (Na, 2.36 wt %, K, 2.09 wt % in Earth's crust) and the likelihood of reducing battery production cost.[8] Further reduction in cost comes from the feasibility of using Al as the anode current collector for NIBs and KIBs instead of the heavier and more expansive Cu often used in LIBs.[9,10]

The fundamental ion storage process in NIBs and KIBs follows the rocking-chair mechanism of LIBs, meaning that ions shuttle back and forth between the anode and the cathode during battery cycles without causing a drastic change in the composition of the electrolyte. Although there are significant benefits to using Na and K chemistries in battery technologies, there exists numerous challenges to

[1] Department of Chemistry, University College London, 20 Gordon Street, London WC1H 0AJ, UK

[2] These authors contributed equally

*Correspondence: y.xu.1@ucl.ac.uk

https://doi.org/10.1016/j.xcrp.2021.100555

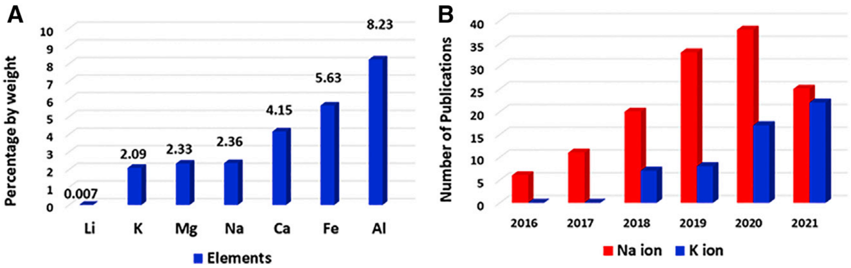

Figure 1. Motivation of and surge in research on metal selenides for NIBs and KIBs

(A) Comparison of the abundance of elements.

(B) Number of publications on metal selenides for NIBs and KIBs published since 2016. Data were collected using the ISI Web of Science. The number in 2021 is limited to the publications from January to May.

deliver high electrochemical performance from NIBs and KIBs. In particular, the higher redox potentials of Na^+/Na and K^+/K compared with Li^+/Li (Na/K/Li: −2.7/−2.9/−3.0 V versus standard hydrogen electrode (SHE) and the larger size of Na^+ and K^+ compared with Li^+ ($Na^+/K^+/Li^+$: 1.09/1.38/0.76 Å) could result in low storage capacity and poor reaction kinetics. The electrochemical performance is primarily determined by electrode materials, and the foremost factor that has rich electrochemistry and aids in achieving high electrochemical performance is the compositional and structural designs of anode materials. Therefore, research on investigating anode materials to store Na^+ and K^+ has been thrust to center stage. Despite the same working principle among LIBs, NIBs, and KIBs, the vast know-how accumulated in the research of Li^+ host materials might not be swiftly applied to Na^+ and K^+ host materials. This could be manifested by the study of graphite, where it was found to be nearly inactive to electrochemically store Na^+ without the cointercalation of electrolyte solvent molecules.[11–13]

Hence, it is of great importance to carry out intensive research on anode materials for NIBs and KIBs. In general, anode materials can be categorized into three types based on their ion storage mechanisms, i.e., intercalation, alloying, and conversion. Intercalation-type anodes, mainly carbon- and titanium-based oxides,[14–17] exhibit good durability but are limited by a low practical capacity and large voltage polarization at high rates because of poor intercalation kinetics.[18] Alloying-type anodes are generally group 14 (Si, Ge, Sn, and Pb) and group 15 (P, Sb, and Bi) elements.[19,20] These anodes have a high theoretical capacity due to multi-electron transfer but are limited by poor cycling stability caused by huge volume expansion. For instance, the alloying reaction of Bi with Na^+ and K^+ leads to volume expansion of 250% and 406%, respectively.[21,22] Conversion-type anodes mainly include metal oxides and chalcogenides.[23,24] They exhibit relatively smaller volume expansion compared with alloying-type anodes and a much higher storage capacity than intercalation-type anodes.

Studies on conversion-type anode materials for NIBs and KIBs have been heavily focusing on metal oxides and metal sulfides.[1,25,26] It was not until recent years that metal selenides (MSs) came into the spotlight. As shown in Figure 1B, the number of publications on MSs has surged since 2016, strongly suggesting rapidly increasing research interest in MSs for NIBs and KIBs (recent reports are summarized in Table 1). Desirable benefits favor MSs. First, MSs have higher electronic conductivity compared with their sulfide counterparts, as seen from the electrical conductivity of Se (1×10^{-3} S m^{-1}) and S (5×10^{-28} S m^{-1}),[27,28] which could result in improved

Table 1. Summary of material and electrochemical performance details of metal selenides recently reported for NIBs and KIBs

Engineering strategy	Material	Structure	NIB/KIB	Voltage range (V)	ICE[a] (%)	Electrolyte	Cycling capacity (mAh g^{-1} @ A g^{-1} @ cycles)	Rate capability (mAh g^{-1} @ A g^{-1})	Storage mechanism	Ref.
Defect	$MoSe_2$	nanosheet assemblies	NIB	0.5–3	92	1.0 M $NaCF_3SO_3$/DEGDME[b]	270 @ 0.1 @ 2,500	220 @ 10	conversion	31
Defect	$Mo(Se_{0.85}S_{0.15})_2$[a]	hollow nanotubes with one closed tip	NIB	0–2.5	82	1.0 M $NaClO_4$/PC[c] (5% FEC[d])	421 @ 0.2 @ 100	370 @ 2	conversion	32
Defect	MoSSe	nanoplates	KIB	0.01–3	78	1.0 M KFSI[e]/EC[f]:DEC[g]	527 @ 0.1 @ 100	310 @ 1	conversion	33
Defect	$MoSe_2$	nanotubes	NIB	0.01–3	72	1.0 M $NaCF_3SO_3$/DGM[h]	260 @ 0.1 @ 200	360 @ 10	conversion	34
Defect	$NiSe_2$/N-doped C	hierarchical hollow microsphere	NIB	0–3	86	1.0 M $NaCF_3SO_3$/PC (5% FEC)	350 @ 0.1 @ 200	380 @ 5	conversion	35
Phase	2H-$MoS_{2x}Se_{2-2x}$	mesoporous nanospheres	NIB	0–3	73	1.0 M $NaClO_4$/PC (5% FEC)	500 @ 0.5 @ 120	180 @ 2	conversion	36
Phase	VSe_2/N-doped C	ultrathin nanosheets	KIB	0–2.5	69	0.6 M KPF_6/EC:DEC	350 @ 0.2 @ 200	220 @ 2	conversion	37
Phase	$CoSe_2$	nanotubes	KIB	0.01–2.5	69	0.8 M KPF_6/EC:DEC	253 @ 0.2 @ 200	220 @ 2	conversion	38
Interlayer spacing	$MoSe_2$/MXene	nanosheets	KIB	0–3	54	1.0 M KFSI/EC:DEC	355 @ 0.2 @ 100	250 @ 10	conversion	39
Interlayer spacing	MoS_2/N,O-doped C	nanotubes	KIB	0–3	44	0.8 M KPF_6/EC:DEC	295 @ 0.25 @ 200	247 @ 1	conversion	40
Interlayer spacing	$MoSe_2$/N-doped C	3D flower-like structure	NIB	0–3	74	1.0 M $NaClO_4$/EC:DEC	350 @ 1 @ 500	320 @ 5	conversion	41
Interlayer spacing	MoS_2/graphene	nanosheets	NIB	0–3	50	1.0 M $NaClO_4$/PC (5% FEC)	1,100 @ 0.1 @ 100	230 @ 51.2	conversion	42
Interlayer spacing	$MoSe_2$	nanosheets	NIB	0.01–3	61	1.0 M $NaClO_4$/EC:DEC	580 @ 0.1 @ 100	400 @ 5	conversion	43
Interlayer spacing	$MoSe_2$	nanosheets	NIB	0.5–3	70	1.0 M $NaClO_4$/PC (5% FEC)	228 @ 1 @ 1,500	200 @ 2	intercalation	44
Interlayer spacing	$MoSe_2$/C	pistachio-shuck-like structure	KIB	0.01–2.5	63	0.8 M KPF_6/EC:DEC	332 @ 0.2 @ 100	250 @ 2	conversion	45
Interlayer spacing	$FeSe_2$	nanorods	NIB	0.5–2.5	95	1.0 M $NaCF_3SO_3$/EC:DMC[i]	520 @ 1 @ 400	110 @ 35	conversion	46
Binary	$NiCoSe_2$	pompon-like structure	NIB	0.5–3	87	1.0 M $NaCF_3SO_3$/DEGDME	284 @ 1 @ 200	200 @ 5	conversion	47
Binary	Co(Ni)Se_2/N-doped C	hollow and porous 3D particles	NIB	0–2.5	65	1.0 M $NaClO_4$/EC:DEC	880 @ 0.1 @ 200	700 @ 1	conversion	48
Binary	$Ni_{1.8}Co_{1.2}Se_4$/N-doped C	nanoaggregates	NIB	0.01–2.8	93	1.0 M $NaClO_4$/EC:PC (5% FEC)	390 @ 0.5 @ 100	180 @ 50	conversion	49

(Continued on next page)

Table 1. *Continued*

Engineering strategy	Material	Structure	NIB/KIB	Voltage range (V)	ICE[a] (%)	Electrolyte	Cycling capacity (mAh g^{-1} @ A g^{-1} @ cycles)	Rate capability (mAh g^{-1} @ A g^{-1})	Storage mechanism	Ref.
Binary	$CoFeSe_2$	nanospheres	KIB	0.01–3	29	1.0 M KFSI/ EC:DEC	273 @ 0.1 @ 200	300 @ 2	conversion	50
Binary	Fe_2CoSe_4	nanospheres	NIB	0.5–2.8	80	1.0 M $NaCF_3SO_3$/ DEGDME	580 @ 4 @ 5,000	400 @ 32	intercalation	51
Binary	$NiCo_2Se_4$[a]	nanoflakes	NIB	0.1–2.5	79	$NaCF_3SO_3$/ EC:PC	378 @ 2 @ 600	450 @ 10	conversion	52
Alloy and defect	Sb_2Se_3	nanorods	KIB	0–3	69	4.0 M KFSI/DME[j]	410 @ 0.1 @ 100	200 @ 10	conversion and alloying	53
Alloy	Bi_2Se_3	curled nanosheets	NIB	0.5–2.9	93	1.0 M $NaCF_3SO_3$/DGM	250 @ 0.1 @ 1,000	400 @ 10	conversion and alloying	54
Alloy	SnSe/N-doped C	nanofibers	NIB	0–3	76	1.0 M $NaPF_6$/ EC:DEC	260 @ 2 @ 700	50 @ 5	conversion and alloying	55
Alloy and composite	Sb_2Se_3/N-doped C/rGO	nanorods	KIB	0.01–3	64	5.0 M KFSI/ EC:DMC	500 @ 0.05 @ 50	180 @ 1	conversion and alloying	56
Alloy and composite	SnSe/N-doped C	nanobelts	NIB	0–3	77	1.0 M $NaPF_6$/ EC:DEC	260 @ 2 @ 200	110 @ 20	conversion and alloying	57
Composite	$NiSe_x$/C	flower-like structure	NIB	0.1–2.8	81	1.0 M $NaCF_3SO_3$/ DEGDME	1,220 @ 0.2 @ 100	370 @ 5	conversion	58
Composite	VSe_2/C	nanorods	NIB	0–3	80	1.0 M $NaClO_4$/ EC:DEC	480 @ 0.2 @ 50	280 @ 4	conversion	59
Composite	$MoSe_2$/C	nanorods	NIB	0.2–3	83	1.0 M $NaClO_4$/ PC (5% FEC)	404 @ 0.2 @ 100	200 @ 5	conversion	60
Composite	$MoSe_2$/C	hollow spheres	NIB	0–3	52	1.0 M $NaClO_4$/ EC:DMC	580 @ 0.2 @ 100	700 @ 3	conversion	61
Composite	CoSe/C,S-doped C	spheres	NIB	0.5–2.8	51	1.0 M $NaCF_3SO_3$/ DEGDME	525 @ 4 @ 10,000	370 @ 8	intercalation	62
Composite	$Co_{0.85}Se$/C	hollow polyhedra	KIB	0.01–2.5	81	1.0 M KFSI/DME	650 @ 0.05 @ 100	250 @ 2	conversion	63
Composite	SnSe/C	nanoboxes	NIB	0–3	75	1.0 M $NaClO_4$/ EC:PC	486 @ 0.1 @ 200	250 @ 5	conversion	64
Composite	$SnSe_2$/rGO	sandwich-like structure	NIB	0–3	88	1.0 M $NaClO_4$/ EC:PC	402 @ 0.1 @ 150	210 @ 10	conversion	65
Composite	$SnSe_2$/C	nanoboxes	NIB	0–3	78	1.0 M $NaCF_3SO_3$/ EC:DMC	580 @ 2.5 @ 200	200 @ 6.3	conversion	66
Composite	FeSe/C	core-shell structure	NIB and KIB	0–3	90 (NIB) and 58 (KIB)	1.0 M $NaCF_3SO_3$/ DEGDME (NIB) and 1.0 M KFSI/ EC:DEC (KIB)	410 @ 1 @ 1,000 (NIB) 660 @ 0.1 @ 1,000 (KIB)	300 @ 10 (NIB) 160 @ 2 (KIB)	conversion	67
Composite	$VSe_{1.5}$/C	nanofibers	NIB	0–3	60	1.0 M $NaClO_4$/ EC:DMC	260 @ 1 @ 500	N/A	conversion	68
Composite	$CoSe_2$/C	nanofibers	NIB	0–3	55	1.0 M $NaPF_6$/ EC:DMC	400 @ 0.2 @ 400	200 @ 15	conversion	69

(*Continued on next page*)

Table 1. *Continued*

Engineering strategy	Material	Structure	NIB/KIB	Voltage range (V)	ICE[a] (%)	Electrolyte	Cycling capacity (mAh g^{-1} @ A g^{-1} @ cycles)	Rate capability (mAh g^{-1} @ A g^{-1})	Storage mechanism	Ref.
Composite	$MoSe_2$/C	nanofibers	NIB	0–3	78	1.0 M $NaClO_4$/ EC:DMC	420 @ 0.5 @ 100	320 @ 3	conversion	[70]
Composite	$CoSe_2$/C	nanofibers	NIB	0.3–3	55	1.0 M $NaClO_4$/ EC:DMC	360 @ 0.1 @ 180	300 @ 2.4	conversion	[71]
Composite	$MoSe_2$/C	nanosheets	NIB	0–3	90	1.0 M $NaClO_4$/ EC:DMC	400 @ 0.2 @ 100	170 @ 5	conversion	[72]
Composite	$FeSe_2$/C	microspheres	NIB	0.01–3	56	1.0 M $NaClO_4$/ EC:DMC	500 @ 0.2 @ 200	500 @ 5	conversion	[73]
Composite	$MoSe_2$/graphene	nanoflowers	NIB	0–4	46	1.0 M $NaClO_4$/ EC:DMC	390 @ 1 @ 100	200 @ 8	conversion	[74]
Composite	$MoSe_2$/rGO	nanosheets	NIB	0–3	65	1.0 M $NaClO_4$/ EC:DEC	750 @ 0.5 @ 100	N/A	conversion	[75]
Composite	WSe_2/rGO	particles	NIB	0–3	72	1.0 M $NaClO_4$/ EC:DMC	250 @ 0.5 @ 100	190 @ 5	conversion	[76]
Composite	$MoSe_2$/graphene	nanosheets	NIB	0–3	95	1.0 M $NaClO_4$/ EC:DEC (5% FEC)	350 @ 0.4 @ 50	350 @ 3.2	conversion	[77]
Composite	NiSe/rGO	nanoparticles	NIB	0–3	80	1.0 M $NaPF_6$/ EC:DMC	400 @ 0.05 @ 50	100 @ 3.2	conversion	[78]
Composite	$MoSe_2$/C	nanoparticles	NIB	0–2.5	58	1.0 M $NaClO_4$/ EC:DMC	300 @ 0.2 @ 250	250 @ 5	conversion	[79]
Composite	$MoSe_2$/C	nanotubes	NIB	0.01–3	75	1.0 M $NaClO_4$/ EC:DMC	450 @ 0.2 @ 100	405 @ 2	conversion	[80]
Composite	ZnSe/C	nanotubes	NIB	0.01–3	55	1.0 M $NaCF_3SO_3$/ DEGDME	380 @ 0.5 @ 100	300 @ 5	conversion	[81]
Composite	$MoSe_2$/C/rGO	nanosheets	NIB	0.01–3	85	1.0 M $NaClO_4$/ PC (5% FEC)	450 @ 0.1 @ 80	300 @ 5	conversion	[82]
Composite	$MoSe_2$@C	nanofibers	NIB	0.01–3	77	1.0 M $NaClO_4$/ EC:DEC	425 @ 0.2 @ 200	350 @ 2	conversion	[83]
Composite	$MoSe_2$/rGO	nanofibers	NIB	0.01–3	63	1.0 M $NaClO_4$/ EC:DMC	500 @ 0.2 @ 350	240 @ 4	conversion	[84]
Composite	$ReSe_2$/C/ graphene	nanofibers	NIB	0.01–3	68	1.0 M $NaClO_4$/ EC:DEC	250 @ 0.2 @ 350	130 @ 2	conversion	[85]
Composite	$MoSe_2$/rGO	nanoparticles	NIB	0–3	78	1.0 M $NaClO_4$/ EC:DEC	390 @ 1 @ 200	50 @ 30	conversion	[86]
Composite	$MoSe_2$/N,P-doped C	nanoparticles	NIB	0.1–2.5	82	1.0 M $NaClO_4$/ PC (3% FEC)	420 @ 0.1 @ 100	260 @ 1	conversion	[87]
Composite	$MoSe_2$/N-doped C/graphene	nanotubes	NIB	0–3	67	1.0 M $NaClO_4$/ EC:DMC	400 @ 1 @ 1,000	300 @ 2	conversion	[88]
Composite	CoSe/N-doped C	nanotubes	KIB	0–3	71	1 M KPF_6/ EC:DEC	300 @ 2 @ 500	300 @ 3	conversion	[89]
Composite	$MoSe_2$/graphene	nanosheets	NIB	0.01–3	63	1.0 M $NaClO_4$/ EC:DMC	370 @ 0.1 @ 500	300 @ 1	conversion	[90]

(Continued on next page)

Table 1. *Continued*

Engineering strategy	Material	Structure	NIB/KIB	Voltage range (V)	ICE[a] (%)	Electrolyte	Cycling capacity (mAh g^{-1} @ A g^{-1} @ cycles)	Rate capability (mAh g^{-1} @ A g^{-1})	Storage mechanism	Ref.
Composite	$MoSe_2$/N,P-doped C	nanosheets	NIB	0.01–3	67	1.0 M $NaClO_4$/EC:DEC	370 @ 0.5 @ 1,000	210 @ 15	conversion	[91]
Composite	$CoSe_2$/C	nanotubes	NIB	0.1–3	63	1.0 M $NaCF_3SO_3$/DEGDME	600 @ 0.1 @ 100	300 @ 2	conversion	[92]
Composite	Fe_7Se_8/C/$MoSe_2$	nanoboxes	NIB	0–3	57	1 M KPF_6/EC:DMC	390 @ 0.1 @ 600	350 @ 1	conversion	[93]
Composite	MoO_2/$MoSe_2$	nanosheets	NIB	0–3	77	1.0 M $NaClO_4$/EC:DEC	410 @ 0.5 @ 300	300 @ 3.2	conversion	[94]
Composite	$SnSe_2$/ZnSe	nanoboxes	NIB	0.1–3	78	1 M $NaPF_6$/DME	430 @ 0.1 @ 200	300 @ 4	conversion	[95]
Composite	$ReSe_2$/N-doped graphene/Ti_3C_2	nanoboxes	KIB	0.01–3	82	1 M KPF_6/EC:DEC	250 @ 1 @ 300	190 @ 10	conversion	[96]
Composite	CuSe/C	nanosheets	NIB	0.1–3	92	1.0 M $NaCF_3SO_3$/DGM	340 @ 0.1 @ 40	300 @ 10	conversion	[97]
Composite	$CoSe_2$/C	nanosheets	NIB	0.1–3	82	1 M $NaPF_6$/DEGDME	320 @ 0.1 @ 100	300 @ 5	conversion	[98]
Interface and composite	$MoSe_2$/N-doped C	nanosheets	KIB	0–3	81	1.0 M KFSI/EMC[k]	300 @ 0.1 @ 100	170 @ 2	conversion	[99]
Interface and composite	FeSe/C	nanorods	KIB	0–3	60	KFSI/EC:DEC	330 @ 0.5 @ 100	290 @ 10	conversion	[100]
Interface	SnSe	nanosheets	NIB	0–3	63	1 M $NaPF_6$/EC:DEC (5% FEC)	300 @ 0.2 @ 100	10 @ 40	conversion	[101]

An intercalation reaction occurs at the initial stage of ion storage for almost all MSs but contributes less capacity than conversion and alloying reactions; hence, intercalation is omitted from "Storage mechanism" for simplicity.

[a] ICE, initial columbic efficiency

[b] DEGDME, diethylene glycol dimethyl ether

[c] PC, propylene carbonate

[d] FEC, fluoroethylene carbonate

[e] KFSI, potassium bis(fluorosulfonyl)imide

[f] EC, ethylene carbonate

[g] DEC, diethyl carbonate

[h] DGM, diglyme

[i] DMC, dimethyl carbonate

[j] DME, dimethyl ether

[k] EMC, ethyl methyl carbonate

reaction kinetics when storing Na^+ and K^+. Second, reaction kinetics could be further improved because as end-discharge products—alkali selenides—have higher ionic conductivity than alkali oxides and sulfides, which are the end-dischage products of metal oxides and sulfides, respectively. This results from the lower energy barrier for ion diffusion in alkali selenides than alkali oxides and sulfides. It has been reported that the Na^+ diffusion energy barriers in Na_2Se, Na_2O, and Na_2S are 0.43, 0.45, and 0.46 eV.[29] Third, the larger size of Se makes the metal-Se bond weaker than metal-O and metal-S bonds, which enables lower polarization[30] during cycles and facilitates reversible conversion reactions. Although Se (679 mAh g^{-1}) has a lower gravimetric capacity than S (1,675 mAh g^{-1}), Se (3,250 mAh cm^{-3}) has a volumetric capacity comparable to that of S (3,470 mAh cm^{-3}) due to the higher density of Se (4.8 g cm^{-3}) compared with S (1.8 g cm^{-3}),[27] which is a crucial factor for modern battery technologies dealing with a limited battery packing space. Therefore, the desirable benefits of MSs provide an appealing foundation to investigate them for NIBs and KIBs.

Given the rapidly increasing research interest in MSs, this review presents an overview of recent progress in developing MS anodes for NIBs and KIBs. We discuss in detail the battery performance improvement of MSs and, more importantly, design strategies for engineering MSs to achieve the improvement, including engineering of defects, interlayer spacing, phases, binary MSs, alloying-based MSs, and composites of MSs, as well as interface engineering with electrolytes, alongside the elucidation of the ion storage mechanisms in MSs. We emphasize that these design strategies are the major driving force of the achieved performance improvement and should be investigated in-depth to keep pushing performance forward. Although there have been a few reviews summarizing metal chalcogenides in batteries,[23,24,102–104] little was explicitly dedicated to MSs in the emerging technologies of NIBs and KIBs, and our approach in this review—a design strategy-directed approach—is different from the material-directed approach presented in those focusing on anodes.[24,102,104] In addition, we discuss the current challenges of employing MSs in NIBs and KIBs, which are derived from critical insights into engineering strategies for MSs, and provide an outlook for future development in this field.

MSs AS ANODES FOR NIBs AND KIBs

Ion storage mechanisms of MSs

The ion storage mechanisms of MSs in NIBs and KIBs are vastly different from selenide to selenide, depending on the crystal structures, the nature of metal cations, and the operating voltage window. In principle, a series of electrochemical reactions could occur when Na^+ or K^+ inserts into selenides over a range of operating voltage windows. At the initial stage of ion insertion, an intercalation reaction occurs, which has been seen in both layered[105,106] and non-layered MSs.[107] The intercalation capability is predominantly determined by the structural feature, with the layered structure showing a higher intercalation capacity than the non-layered structure, which is presumably because there are more available sites for ions to reside between the layers. Subsequent ion insertion with an increasing discharge depth typically follows two mechanisms, depending on the nature of metal cations. First, if the metal in the selenide is electrochemically inactive, a conversion reaction takes place to form an alloy with Na^+/K^+. This results in the reduction of the selenide, forming a metal phase and sodium/potassium selenides. Second, if the metal is electrochemically active, an alloying reaction takes place after the conversion reaction to form an alloy with Na^+/K^+. This results in the presence of sodium/potassium-metal alloys in various stoichiometries and sodium/potassium selenides, delivering a high capacity because of the extra step of alloying. Because conversion and/or alloying reactions often dominate the capacity of MSs, the following discussion in this section omits the intercalation reaction, but keep in mind that it indeed contributes to the capacity of MSs.

The mechanism of the conversion reaction is based on the reduction of metal cations and involves multiple electron transfer. Representative MSs following this mechanism include Mo, V, W, Co, Fe, Ni, and Re selenides. The following equation describes the general reaction of ion storage:

$$M_xSe_y + yzA^+ + yze^- \rightarrow xM + yA_zSe, \qquad \text{(Equation 1)}$$

where M and A represent metal and Na or K, respectively; x and y indicate the stoichiometry of the chemical composition of the MS; and z is the number of the reactions between the combined A^+ and Se ($2 \le y \le 8$, where y significantly depends on reaction kinetics). M and A_zSe are formed after the first discharge process, and the metallic phase M can form a continuously conductive network embedded in the mixed phases, which increases the electronic conductivity of the mixture. During the first charge process, M is oxidized while A^+ is released from A_zSe, thereby regenerating M_xSe_y. The conversion reaction of MSs could be partially reversible, and various species that are different from the pristine selenide, such as metal selenides with a stoichiometric ratio other than x/y and sodium/potassium polyselenides due to the incomplete desodiation/depotassiation of A_zSe, could be found at the end of the charge process.[23]

The mechanism of conversion and alloying reactions involves multiple electron transfer from both reactions and generally provides a higher capacity than the conversion mechanism. The metals constituting such MSs are usually group 14 and 15 metals such as Sn, Sb, Bi, and Ge. Zn has been reported to form an alloy with Na^+ in studies of ZnSe,[108] but the alloy contains a very low amount of Na^+ ($NaZn_{13}$) and hence contributes little to the overall capacity. The following equations describe the general reactions of ion storage:

$$M_xSe_y + yzA^+ + yze^- \rightarrow xM + yA_zSe, \qquad \text{(Equation 2)}$$

$$xM + wA^+ + we^- \rightarrow A_wM_x, \qquad \text{(Equation 3)}$$

where w is the number of A^+ reacting with M via the alloying reaction. During the initial discharge process, M and A_zSe are formed in the same way as described in the conversion mechanism. With increasing discharge depth, the A_wM_x alloy clusters are generated and entangled with A_xSe, forming an aggregation of the two compounds at the end of the discharge process. Upon a full charge process, A^+ is extracted from A_wM_x and A_xSe, resulting in the reappearance of M_xSe_y. However, only a portion of A_wM_x and A_xSe could contribute to the reappearance of M_xSe_y, and it is highly possible to observe various phases at the end of the charge process, such as MSs with a stoichiometric ratio other than x/y, sodium/potassium polyselenides due to the incomplete desodiation/depotassiation of A_zSe, and even Na/K-M alloys with a stoichiometric ratio other than w/x due to the incomplete de-alloying process of A_wM_x. The ion storage process of this type of MSs is worth carefully investigation by engineering the microstructures and compositions of MSs, which could solve issues associated with the unique phase transitions. Such investigation are exemplified in alloy engineering.

The Na^+/K^+ storage mechanism in MSs can be studied using a range of *ex situ* and *in situ* characterization techniques, to which we exemplify a few reports in this section. *In situ* Raman and *ex situ* transmission electron microscopy (TEM) were complementarily employed to study the potassiation and depotassiation of $MoSe_2$.[109] The Raman peak at 244.4 cm^{-1}, which belongs to the A_{1g} mode, gradually shifted to 247.5 cm^{-1}

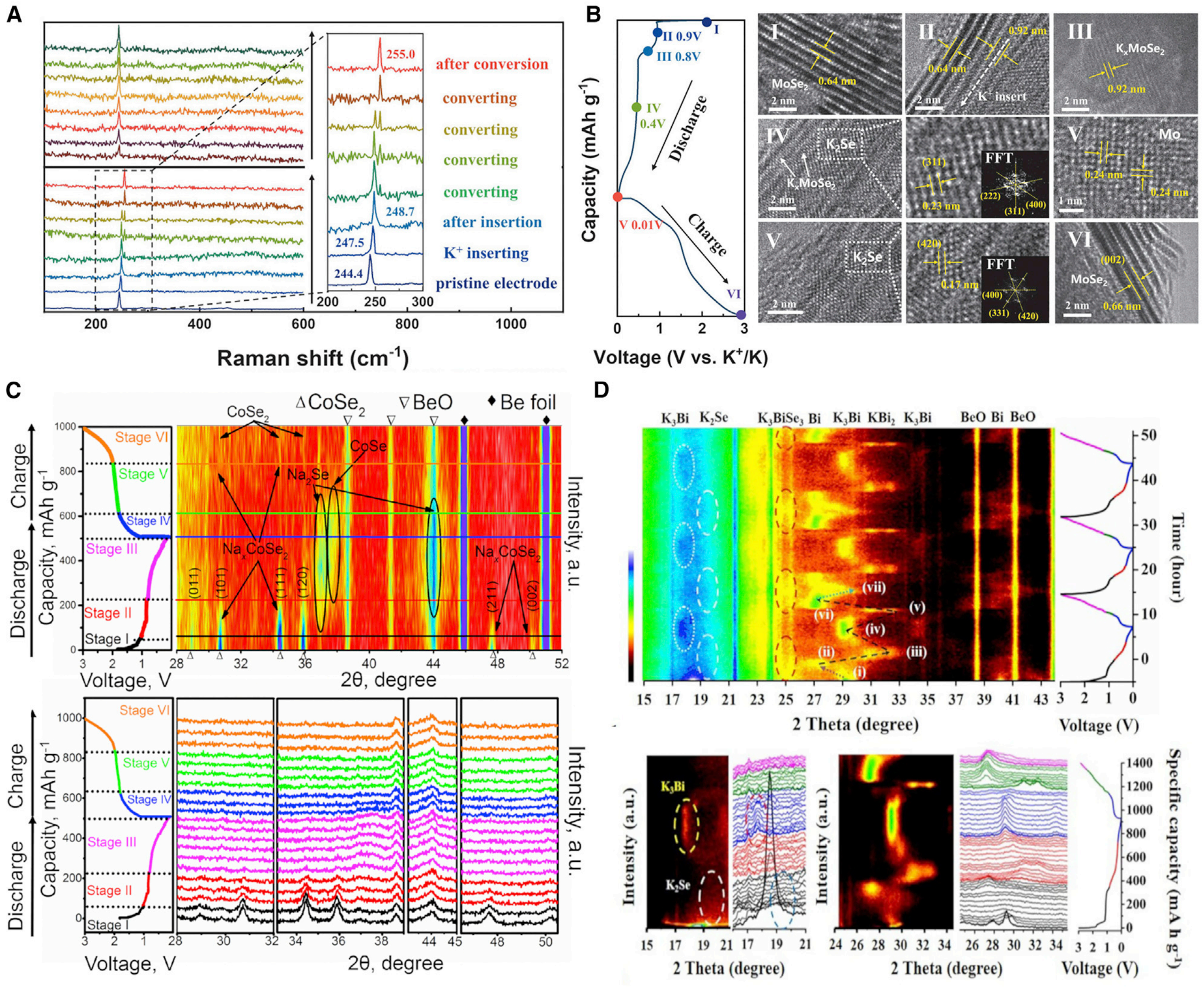

Figure 2. Mechanistic investigation of MSs using *in situ* characterization

(A) *In situ* Raman spectra of the $MoSe_2$ electrode during discharge and charge processes in KIBs.

(B) *Ex situ* HRTEM images of the $MoSe_2$ electrode at different stages of the first cycle. Reproduced with permission.[109] Copyright 2020, Wiley-VCH.

(C) *In situ* XRD patterns and contour plots of the $CoSe_2$ electrode at the range of 0.01–3.0 V during the initial cycle of NIBs and selected diffraction patterns during the initial cycle stacked against the voltage profile. Reproduced with permission.[110] Copyright 2017, Elsevier.

(D) *In situ* XRD patterns and corresponding line plots of the Bi_2Se_3 electrode in KIBs. Reproduced with permission.[111] Copyright 2021, Elsevier.

during K^+ intercalation into the $MoSe_2$ layers (Figure 2A) and eventually shifted to 248.8 cm^{-1} at the end of the intercalation, forming K_xMoSe_2. Meanwhile, a small peak appeared at 255 cm^{-1}, indicating that K_xMoSe_2 started to convert to the final discharge product K_2Se. When the voltage was decreasing toward 0.01 V, the K_xMoSe_2 peak intensity continued to decrease while the K_2Se peak intensity continued to increase until the K_xMoSe_2 peak disappeared at 0.01 V. The *ex situ* high-resolution TEM (HRTEM) results (Figure 2B) showed that the interlayer spacing of the initial $MoSe_2$ increased from 0.64 to 0.92 nm with the decrease of voltage during the discharge process, corresponding to the formation of K_xMoSe_2. K_2Se appeared between the K_xMoSe_2 layers when the voltage reduced to 0.4 V, and the lattice fringes of K_2Se and Mo can be observed at 0.01 V. *In situ* X-ray diffraction (XRD) was used to demonstrate the formation of new phases when applying $CoSe_2$ as an anode for NIBs (Figure 2C).[110] After initial Na^+ intercalation (stage I) to form

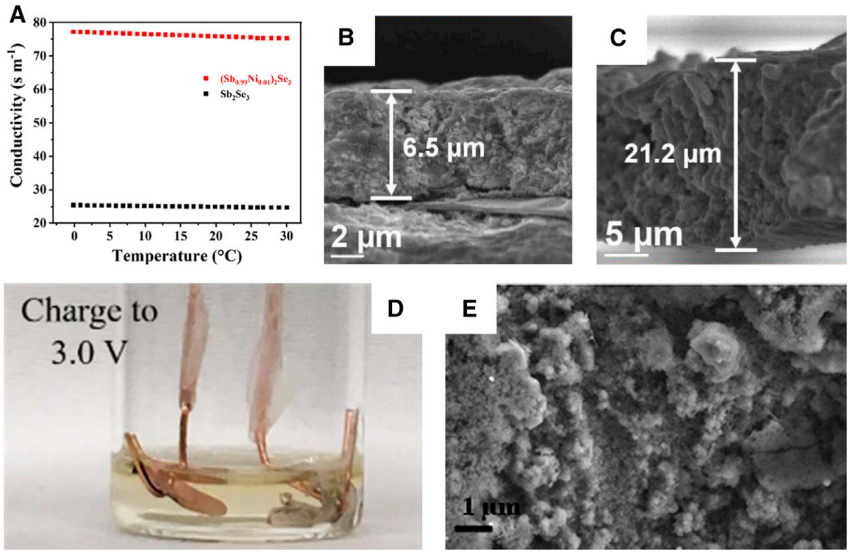

Figure 3. Challenges of using MSs for NIBs and KIBs

(A) Electronic conductivity of Sb_2Se_3 and Ni-doped Sb_2Se_3. Reproduced with permission.[53] Copyright 2020, Wiley-VCH.

(B and C) Cross-section SEM images of the Sb2Se3 anode before cycling (B) and after 8 cycles (C). Reproduced with permission.[56] Copyright 2020, Wiley-VCH.

(D) Digital photo of the bottle-type cell of $MoSe_2$/graphene after charging to 3.0 V. Reproduced with permission.[94] Copyright 2018, Elsevier.

(E) SEM image of the ZnSe@C electrode after 100 cycles. Reproduced with permission.[112] Copyright 2021, Elsevier.

Na_xCoSe_2, new phases of Na_2Se and CoSe were formed between 1.1 and 0.8 V (stage II), which was indicated by the appearance of peaks at 37.2° and 37.5°, respectively. Continuing the discharge toward 0.01 V (stage III), the Na_xCoSe_2 peak gradually disappeared with increasing peaks of Na_2Se at 37.2° and 43.9°, and Co metal was formed at the end of the discharge process. The reactions were reversed during the subsequent charge process (stages IV, V, and VI); however, the diffraction peaks of $CoSe_2$ became weakened and broadened because of pulverization and structural transformation during the process. *In situ* XRD was also used to study the conversion and alloying processes of the KIB anode Bi_2Se_3 (Figure 2D).[111] It was found that during the conversion reaction to generate Bi and K_2Se (stage i to ii), the phase of K_3BiSe_3 was identified by peaks at 25.4°, 28.5°, and 41.2°, suggesting that the reaction was carried out with an intermediate product in two consecutive steps. During continuous discharging to 0.01 V, Bi was alloyed with K to form first KBi_2 (stage ii to iii) and then K_3Bi (stage iii to iv), indicating that the alloying reaction was completed.

Challenges of using MSs in NIBs and KIBs

Despite great efforts devoted to identifying MSs and improving their performance as anode materials for NIBs and KIBs, it is still an emerging research field, particularly for KIBs, and there are challenges to overcome:

(1) Some MSs have intrinsically low electronic and ionic conductivity. This hinders electron transfer and ion insertion/diffusion and often results in sluggish reaction kinetics, large electrochemical polarization, limited ion storage capacity, and even partially electrochemical inactivity of the materials. In addition, the large size of Na^+ and K^+ over Li^+ makes high ionic conductivity more critical when applying MSs in NIBs and KIBs compared with LIBs. In a study of

Sb_2Se_3 for KIBs,[53] the electronic conductivity of Sb_2Se_3 was measured to be $\sim$25 s m^{-1} by a four-probe method (Figure 3A) and its K^+ diffusion coefficient (D_K) was in the range of 10^{-15}–10^{-11} cm^2 s^{-1}. The low electronic and ionic conductivity (indicated by D_K) resulted in a >80% capacity loss in just 40 cycles at 100 mA g^{-1} and a capacity of <100 mAh g^{-1} at a moderate rate of 1 A g^{-1}.

(2) MSs undergo large volume change during conversion reactions, and some experience huge volume expansion if alloying reactions are involved to store Na^+/K^+. The large volume change can induce an irreversible phase change, reduce the utilization of MSs, and in some cases make electrochemically active sites and/or electrochemical reactions inaccessible. This can cause capacity decay and structural instability. The huge volume expansion during an alloying reaction can cause electrode cracking and delamination from the current collector, leading to cell failure. As exemplified by a conversion and alloying anode Sb_2Se_3,[56] the thickness of the Sb_2Se_3 electrode film increased by 133.8% after the first discharge. Even with carbon encapsulation and/or confinement, the increase in thickness still reached 80.3% and 105.8% with the presence of N-doped carbon and reduced graphene oxide (rGO), respectively. The increase remained high after 8 charge-discharge cycles and the film was 3.3, 2.2, and 1.6 times thicker than the pristine state for no carbon (Figures 3B and 3C), N-doped carbon, and reduced graphene oxide, respectively. This suggested not only that the volume of the Sb_2Se_3 electrodes expanded substantially in the initial cycle but also that the expansion remained in the following cycles. As a result, the three electrodes exhibited significant capacity loss after the first 20 cycles at 50 mA g^{-1}, with the Sb_2Se_3 and Sb_2Se_3@N-doped carbon electrodes showing nearly zero capacity.

(3) It is recognized that the dissolution of polyselenides in electrolytes and the detrimental shuttle effect occur when employing MSs in NIBs and KIBs, which was indicated by the discharge intermediate products in the previous discussion. The shuttle effect can dramatically reduce capacity, deteriorate cycling stability, and lower columbic efficiency (CE). It is highly possible that the dissolved polyselenides migrate to Na/K metal and cause side reactions to deposit Na_2Se/K_2Se that passivates the metal, which not only blocks Na^+/K^+ diffusion on the metal side but also depletes the MS in the cell. It has been experimentally observed that deposits were found on the surfaces of both the separator and the Na counter electrode in a NIB half-cell where $MoSe_2$-graphene was tested against Na,[94] indicating a severe shuttle effect of soluble $NaSe_n$. This was proved in a visible bottle-type cell, in which the colorless electrolyte changed to orange-red after charging $MoSe_2$/graphene to 3.0 V (Figure 3D), which resulted from the formation of $NaSe_n$ and its dissolution in the electrolyte (as discussed in composites with compounds). One may argue that there is no metal present in a NIB/KIB full cell, but polyselenides can migrate toward the cathode side and be reduced to Na_2Se/K_2Se that deposits on the cathode, which in a same way depletes the MS anode in the full cell.

(4) Large volume change and dissolution of polyselenide can both contribute to the destabilization of the solid-electrolyte interphase (SEI) formed on the surface of MSs. Repetitive volume expansion and compression disrupt the existing SEI generated from previous cycles and expose the fresh surface of MSs to the electrolyte, forming new SEI on the fresh surface. This accelerates the consumption of ions in the cell and can be the reason for slowly increased CE and side reactions involving MSs. Taking ZnSe@C as an example of NIB anodes, the C 1 s X-ray photoelectron spectroscopic results tested at different charge-discharge states gave a strong indication of a thick SEI and its instability.[112] When

discharged to 0.5 V, the position of the C=O peak shifted toward a high-binding energy direction and its identity significantly increased, suggesting that C=O was converted to O-C=O because of the decomposition of electrolyte (1 M $NaCF_3SO_3$ in diglyme) and the formation of a thick SEI. When charged back to 1.7 and 3.0 V, the C=O, O-C=O, and CF_3 species further increased compared with the discharge process, indicating the destabilization of the existing SEI formed in the discharge process. This eventually led to the rampant structure of ZnSe@C after 100 cycles, which was different from the original structure (Figure 3E). Nanostructures tend to have a large surface area and consequently a high possibility of the SEI being disrupted, so the destabilization of SEI could be more critical for nanostructures compared with bulk selenides.

ENGINEERING STRATEGIES FOR MSs FOR NIBs AND KIBs

Defect engineering

Engineering crystallographic defects is an effective approach to shape the physical and chemical properties of electrode materials. It has been proven that defect sites can act as storage/adsorption/active sites to anchor foreign ions or intermediate species in the process of storing ions and, as a result, increase the capacity of MSs.[31] Defects can also change the atomic structure and charge distribution of MSs and thus enhance the kinetics of ion diffusion and electron transfer, which often results in improved rate capability.[32]

Among various types of defects, vacancies are one of the most studied types in the field of batteries.[113] Oxygen vacancies have received great attention because they optimize the ion storage performance of a range of oxide electrodes available in NIBs and KIBs.[5] Another type of anion vacancy, selenium vacancy, has started gaining attention because of the rapidly increasing number of studies on selenide electrodes.[33,34] He et al.[33] reported on $MoS_{2(1-x)}Se_{2x}$ nanoplates with anion vacancies that were derived by partially substituting Se in $MoSe_2$ with S. The substitution level of S in $MoS_{2(1-x)}Se_{2x}$ was adjusted via the molar ratio of S over the $MoSe_2$ precursor in a vacuum annealing process, which in turn tuned the vacancy concentration in $MoS_{2(1-x)}Se_{2x}$. The authors ascribed the formation of the vacancies to the increased disorder and distortion in the layered structure when two anions coexisted in the lattice (Figure 4A). Among several S:Se ratios (1:3, 1:1, and 3:1), MoSSe (S:Se = 1:1) showed the highest concentration of anion vacancies and, when tested as a KIB anode, exhibited the highest initial CE (ICE) (77.9%), the highest initial capacity (547.1 mAh g^{-1}), the best cyclability (96.3% after 100 cycles) at 100 mA g^{-1}, and the best rate capability (263.2 mAh g^{-1} at 5 A g^{-1}) among the three ratios (Figure 4B). The kinetic study showed that compared with MoS_2 and $MoSe_2$, MoSSe exhibited a greater capacitive contribution and a higher D_K (Figure 4C), suggesting that the presence of anion vacancies improved the reaction kinetics of potassiation or depotassiation. This was supported by density functional theory (DFT) simulations that suggested improved electronic conductivity of MoSSe and its increased active sites energetically favorable for K adsorption. Lattice defects are often found in materials with a low crystallinity and/or disordered structure.[114] Li et al.[34] synthesized highly disordered $MoSe_2$ layers embedded in a P- and N-co-doped carbon matrix via a two-step reaction (Figure 4D), in which Se nanorods were used as the shape-directed agent and *in situ* selenization resources to form hybrid nanotubes ($MoSe_2 \subset$PNC-HNTs). The nanotubes had unique walls in which highly disordered $MoSe_2$ layers were dispersed (Figures 4E and 4F). The authors speculated that the formation of the disordered layers could be associated with the limited Se source that cannot well achieve crystallized layers. $MoSe_2 \subset$PNC-HNTs were employed as anode

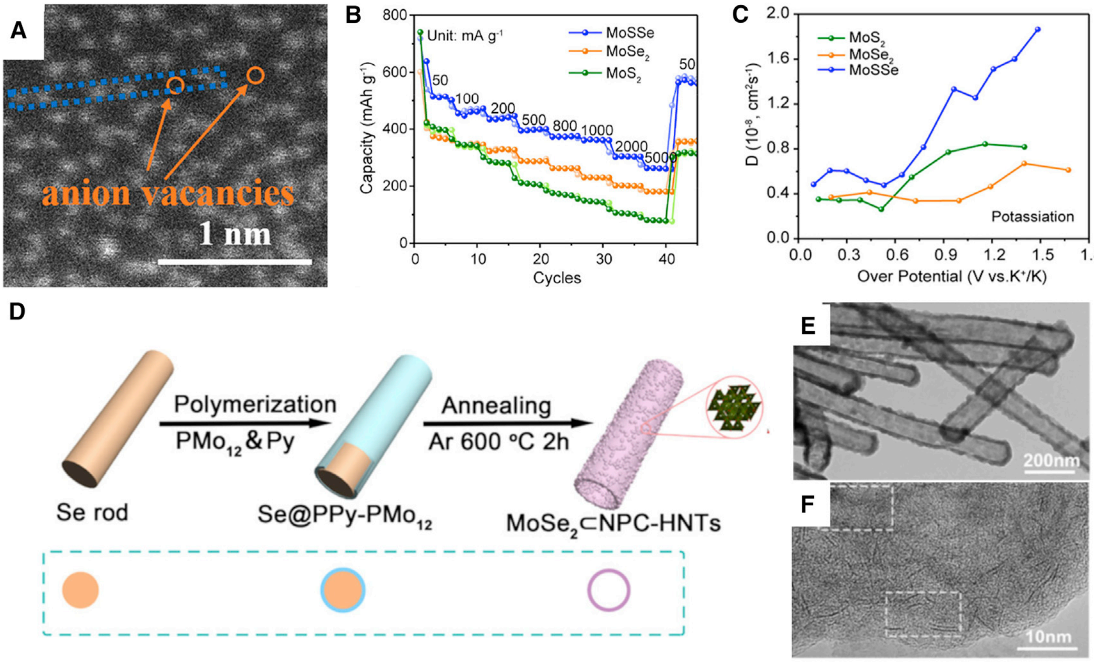

Figure 4. Defect engineering in MSs for NIBs and KIBs

(A) High-resolution scanning transmission electron microscopy (HR-STEM) image of MoSSe (S:Se = 1:1).

(B) Rate capability of $MoS_{2(1-x)}Se_{2x}$ in KIBs.

(C) D_K of MoS_2, MoSSe, and $MoSe_2$, calculated from the potential profiles of the galvanostatic intermittent titration technique. Reproduced with permission.[33] Copyright 2019, American Chemical Society.

(D) Schematics of the synthesis process of $MoSe_2 \subset$PNC-HNTs.

(E and F) TEM (E) and HRTEM (F) images of $MoSe_2 \subset$PNC-HNTs. Reproduced with permission.[34] Copyright 2020, American Chemical Society.

materials for both NIBs and KIBs. They exhibited high specific capacities of 280 and 262 mAh g^{-1} over 200 cycles at 0.1 A g^{-1} for Na^+ and K^+ storage, respectively, and capacity retention rates of 87% at 2 A g^{-1} over 3,500 cycles for Na^+ storage and 80% at 1 A g^{-1} over 500 cycles for K^+ storage. Major contributors to the great performance were that the highly disordered $MoSe_2$ layers enabled many active sites that facilitated capacitive-controlled ion storage kinetics and the wall structure provided excellent mechanical properties, which was supported by the intact structure after 200 cycles at 0.1 A g^{-1} for NIBs. Besides low crystallinity and disordered structures, defects can form in crystal boundaries and hence increase active sites to store ions. Polycrystalline $NiSe_2$ was reported to be composed of numerous microcrystals,[35] in which the rich crystal boundaries between the microcrystals led to the increase of active sites and defects and facilitated the triggering of redox reactions. Rich crystal boundaries might lead to high exposure of the electrode's surface area to electrolytes, which in turn leads to a low ICE. As seen in the same report, polycrystalline $NiSe_2$ exhibited a lower ICE (71%) than its highly crystalline counterpart (86%).

Phase engineering

The inherent conductivity of MSs plays an important role in their electrochemical performance. By changing the phase of MSs, conductivity can be dramatically improved and even reach the level of a metallic phase. The two-dimensional (2D) transition metal selenides MSe_2 (M = Ti, V, Nb, Mo, W, and Re) have a unique layered structure characterized by strong in-plane covalent bonding within the Se-M-Se layers and a weak van der Waals interaction between neighboring layers. The

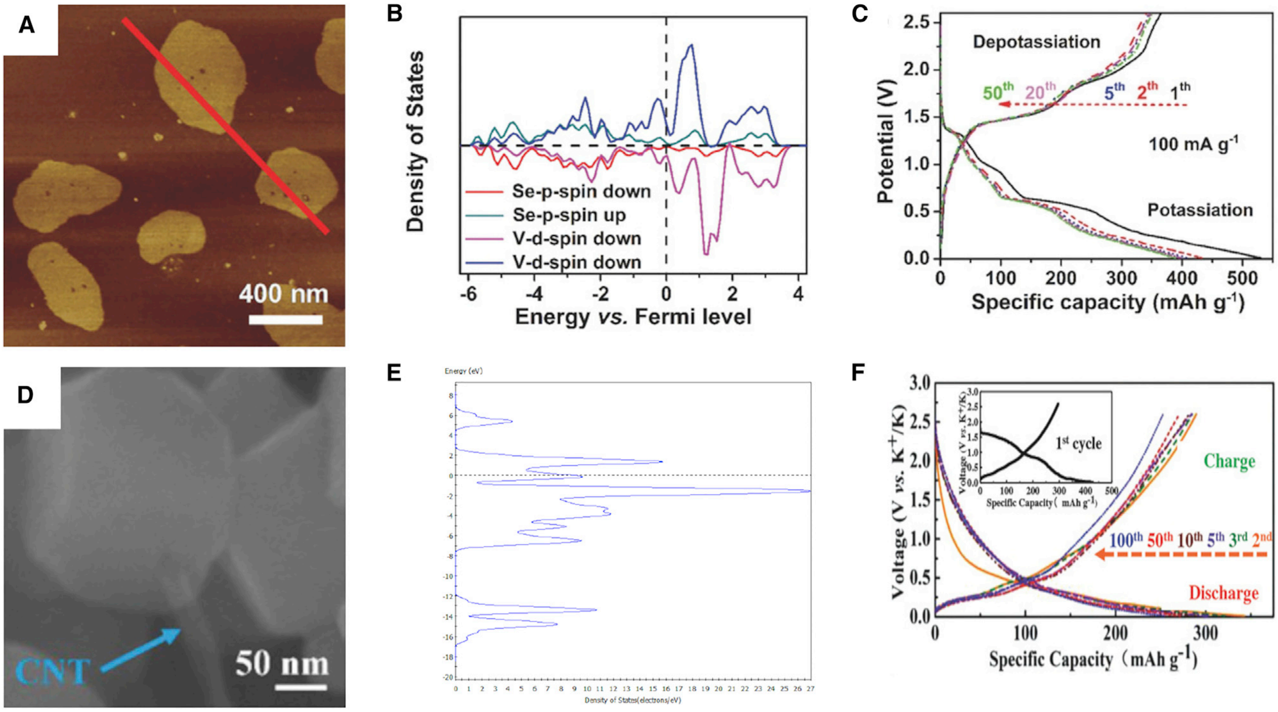

Figure 5. Phase engineering in MSs for NIBs and KIBs

(A) Atomic force microscopy (AFM) image of individual VSe_2 nanosheets.

(B) Calculated spin-polarized projected density of states of V and Se in bulk VSe_2.

(C) Charge-discharge curves of VSe_2 nanosheets at 100 mA g^{-1} in KIBs. Reproduced with permission.[37] Copyright 2018, Wiley-VCH.

(D) Scanning electron microscopy (SEM) image of $CoSe_2$/N-doped carbon nanotubes.

(E) Band-gap structure of $CoSe_2$.

(F) Charge-discharge curves of $CoSe_2$/N-doped carbon nanotubes at 0.2 A g^{-1} in KIBs (inset is the curves in the first cycle). Reproduced with permission.[38] Copyright 2018, Wiley-VCH.

polymorphic structure of MSe_2 is determined by the coordination and stacking order of the metal atoms. There are three types of coordination of the metal atoms, namely, triangular prism, octahedron, and twisted octahedron coordination, which are regarded as the 1T, 2H, and 3R phases of MSe_2, respectively.[103] Due to the significant differences in physical and chemical or electrochemical properties between the phases, tuning the phases of MSe_2 metal selenides is a straightforward but powerful strategy to engineer their battery performance. Zhang et al.[36] recently reported phase engineering of $MoSe_2$ from the 1T to the 2H phase. 1T $MoSe_2$ was obtained after a solvothermal reaction, but it transformed to 2H $MoSe_2$ after annealing at 600°C for 1 h in an Ar/H_2 (5% H_2) atmosphere and kept the 2H phase after sulfurization ($MoS_{2x}Se_{2-2x}$). Graphene-like VSe_2 nanosheets were synthesized with an average thickness of about 3.08 nm (Figure 5A).[37] The calculated spin-polarized projection state density showed that VSe_2 was metallic and had a relatively large electronic state at the Fermi level (Figure 5B). The structure with a small atomic layer thickness was highly conducive to interface storage and can promote the transmission of alkali metal ions and electrons across the material. Tested as an anode in KIBs, the charge and discharge curves (Figure 5C) almost coincided between the 5th and the 20th cycles, except for the capacity loss after the initial discharge because of the formation of the SEI layer. This resulted from the metallic nature of VSe_2 nanosheets enabling high electronic conductivity and their submicron-level lateral size and sufficient buffer space between nanosheets buffering the volume change during repeated cycles and helping to maintain structural integrity. Similarly, metallic $CoSe_2$ was reported with the highly conductive N-doped carbon nanotubes (CNTs) as a flexible framework and applied as a high-performance KIB anode.[38] The metallic $CoSe_2$ was in an octahedral shape and arranged in sequence along the carbon nanotubes (Figure 5D), and the zigzag-shaped void space can adapt to the volume expansion during cycles. A zero band gap can be seen in the band structure analysis (Figure 5E), which indicated the metallic nature and high conductivity of the obtained $CoSe_2$. The charge and discharge capacities in the initial cycle were 296 and 427 mAh g^{-1} (Figure 5F), respectively, resulting in an ICE of 69.3%. The curves largely overlapped after 10 cycles, when a stable and strong SEI layer was formed. The unique metallic phase of $CoSe_2$ resulted in a high capacity of 253 mAh g^{-1} at 0.2 A g^{-1} after 100 cycles and a rate performance of 173 mAh g^{-1} at 2 A g^{-1} after 600 cycles.

Interlayer spacing engineering

Expanding the interlayer spacing of MSs is another effective strategy to reduce the ion diffusion energy barrier and improve ion diffusion kinetics, as well as accommodate volume change during ion insertion/extraction.[39] The synthetic method commonly used to expand interlayer spacing uses compounds that contain amine groups (e.g., ethylenediamine,[40] ammonium citrate,[41] and hydrazine hydrate[42,46]) as reducing agents, in which the gas molecules released from the decomposition of the compounds during the reaction intercalate in the space between MS layers. Zheng et al.[41] prepared $MoSe_2$/carbon composites using a hydrothermal reaction, in which carbon sources (ammonium citrate and citric acid) opened $MoSe_2$ layers and restricted the restacking of $MoSe_2$ nanosheets, resulting in few-layered $MoSe_2$ with expanded interlayer spacing. The average layer number in $MoSe_2$/N-doped carbon nanosheets ($MoSe_2$/CN, with ammonium citrate as the carbon source) was 3–6 layers, and the interlayer spacing of $MoSe_2$ was 0.75 nm (Figure 6A), compared with 7–8 layers and 0.68 nm interlayer spacing in $MoSe_2$/carbon ($MoSe_2$/C, with citric acid as the carbon source). It was speculated that the interlayer expansion was caused by the gas molecules of CO_2, H_2O, and NH_3 formed during the decomposition of the carbon sources, and more gases were formed from ammonium citrate than citric acid, which caused larger interlayer spacing in $MoSe_2$/NC than $MoSe_2$/C. The speculation was supported by the control sample $MoSe_2$ that exhibited interlayer spacing of 0.65 nm and stacking of 9–10 layers without the involvement of carbon. When tested as a NIB anode, $MoSe_2$/CN exhibited a capacity retention of 88.5% after 500 cycles at 1 A g^{-1}, as opposed to 68.2% for $MoSe_2$/C and nearly complete capacity loss for $MoSe_2$. In addition, $MoSe_2$/CN delivered 523.6, 407.4, 370, 347, 326, 310.2, and 300.1 mAh g^{-1} at 0.1, 0.5, 1, 2, 3, 4, and 5 A g^{-1}, respectively (Figure 6B). Post-cycling characterization (Figure 6C) showed that the interlayer spacing of $MoSe_2$/CN had no major change, whereas pulverization and restacking into thicker sheets were observed in $MoSe_2$/C and $MoSe_2$, indicating a highly stable structure of $MoSe_2$/CN to effectively adapt to the volume expansion of $MoSe_2$ nanosheets. Tang et al.[43] fabricated carbon-stabilized interlayer-expanded $MoSe_2$ nanosheets ($MoSe_2$@C) by oleic acid functionalized synthesis with a polydopamine (PDA) stabilization-carbonization strategy. $MoSe_2$@C showed a petal-like structure, and the interlayer spacing of $MoSe_2$ was expanded to 0.7 nm (Figure 6D), larger than that of bulk $MoSe_2$ (0.64 nm). The authors attributed the extended interlayer spacing to the unique coordination of Mo atoms with oleic acid during the synthesis. When $MoSe_2$@C was assembled into a NIB full cell (with $Na_3V_2(PO_4)_3$ as the cathode material), the cell showed a high capacity of 421 mA h g^{-1} at 0.2 A g^{-1} after 100 cycles (Figure 6E). The unique carbon-stabilized interlayer expanded nanosheet structure facilitated the penetration of the electrolyte into the nanosheets and improved the charge transfer efficiency between $MoSe_2$ nanosheets. In another study, a simple

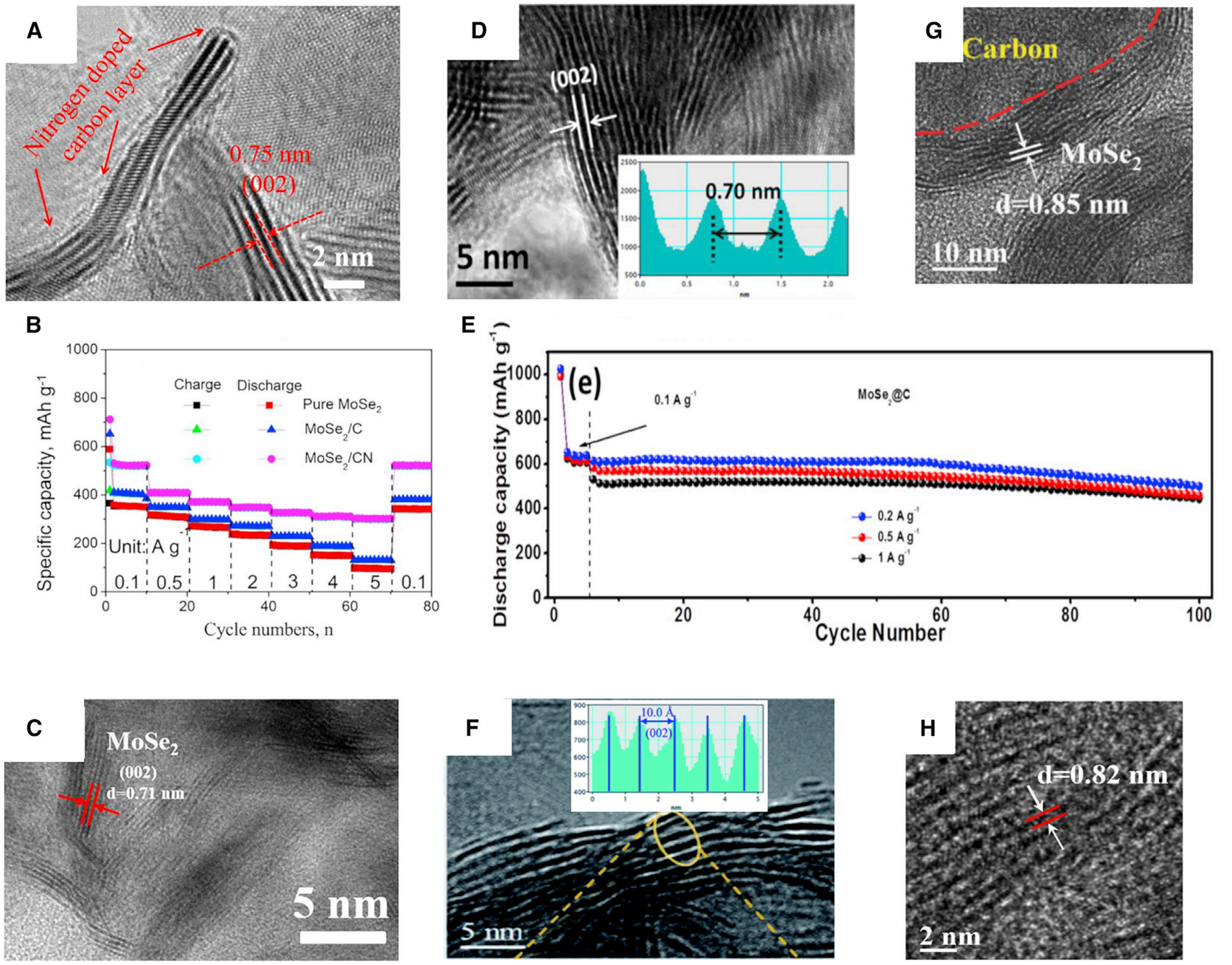

Figure 6. Interlayer spacing engineering in MSs for NIBs and KIBs

(A) HRTEM image of $MoSe_2$/CN.

(B) Rate capability of $MoSe_2$, $MoSe_2$/C, and $MoSe_2$/CN in NIBs.

(C) HRTEM image of the $MoSe_2$ electrode discharged to 0.01 V. Reproduced with permission.[41] Copyright 2019, Elsevier.

(D) HRTEM image of $MoSe_2$@C.

(E) Cycling stability of $MoSe_2$@C in the voltage range of 0.01–3 V in NIBs. Reproduced with permission.[43] Copyright 2016, American Chemical Society.

(F) HRTEM image of $MoSe_2$ nanotubes. Reproduced with permission.[44] Copyright 2017, Royal Society of Chemistry.

(G and H) HRTEM images of PMC. Reproduced with permission.[45] Copyright 2018, Wiley-VCH.

hydrothermal with a mixture of octylamine and ethanol as the solvent was used to obtain $MoSe_2$ with even larger interlayer spacing of about 1 nm (Figure 6F).[44] This resulted from the intercalation of the ammonia species originating from the octylamine molecules during the hydrothermal reaction, which was suggested by the similarity between the expansion of the gallery height (0.354 nm) and the diameter of the ammonia species (~0.35 nm). Such large interlayer expansion, combined with several $MoSe_2$ layers, was expected to lower the energy barrier of Na^+ intercalation and diffusion and increase the accessible active surface area to the electrolyte.

Interlayer expansion could be even more critical in KIBs, because K^+ has a larger size than Na^+. Wang et al.[45] synthesized $MoSe_2$ nanostructures using oleylamine as the solvent and attributed the expansion of interlayer spacing to the intercalation of ammonium molecules derived from oleylamine. The obtained pistachio-shuck-like

$MoSe_2$/C core-shell (PMC) nanostructures showed interlayer spacing of >0.8 nm (Figures 6G and 6H). The expansion increased the gallery height from 0.31 nm for bulk $MoSe_2$ to 0.51 nm, which can reduce the energy barrier for K^+ insertion/diffusion and increase the number of exposed active sites for K^+ adsorption. PMC displayed a high reversible capacity of 322 mAh g^{-1} after 100 cycles at 0.2 A g^{-1}, corresponding to a capacity retention of 83.9%, and retained 224 mAh g^{-1} at 2 A g^{-1}. PMC showed nearly unchanged charge transfer resistance from the 5th to 100th cycle, and its high capacitive charge storage contribution was calculated to be 76%. Theoretical simulations suggested that the energy barrier of K^+ diffusion was much lower on the surface of the $MoSe_2$ layer than in the bulk of $MoSe_2$. Although K^+ diffusion behavior in interlayer expanded $MoSe_2$ might differ from that of a single $MoSe_2$ layer (representing indefinite interlayer expansion), the simulation results qualitatively proved more energetically favorable K^+ migration in PMC than bulk $MoSe_2$.

Engineering binary selenides

Binary MSs consisting of two metal elements have received extensive attention because of their higher conductivity and better electrochemical activities compared with their mono-metal counterparts.[47] Studies have proven that binary MSs have plentiful phase interfaces and rich redox chemistry, which could lower the activation energy of ion migration and accelerate reaction kinetics, thus enhancing electrochemical performance.[48] The major drawback of binary MSs is the large volume expansion during the charge and discharge processes, as experienced by many other electrode materials that undergo a conversion reaction to store ions. In this regard, strategies have been applied to engineer nanostructures of binary MSs in carbon matrices. Widespread attention has been given to the spinel structure of $A_xB_{3-x}Se_4$, where A and B are a binary combination of Fe, Co, or Ni,[49] together with a few cases of compositional variations such as $CoMoSe_4$.[115]

An impregnation method was used to synthesize ultrafine Co-Fe binary selenides embedded in hollow mesoporous carbon nanospheres (HMCSs) as KIB anode materials.[50] The method involved loading Co and Fe precursors into HMCS templates and subsequent selenization to convert the mixed precursors to binary selenides impregnated in HMCSs. By controlling the selenization temperature, it was possible to control not only the composition of the binary selenides but also the nanostructures of the composites, from $(Co_{0.5}Fe_{0.5})_{0.85}Se$ hollow spheres (CFSe/C-250) at 250°C to $(Co_{0.5}Fe_{0.5})Se_2$ hollow spheres (CFSe/C-300) at 300°C and further to $(Co_{0.5}Fe_{0.5})_3Se_4$ frog-egg-like structures (CFSe/C-500) at 500°C (Figure 7A). Using CFSe/C-300 as an example, the total resistance calculated from the *in situ* electrochemical impedance spectroscopy (EIS) measurement was found to significantly decrease before reaching 0.7 V during the initial discharge process, which suggested the ultrafine metallic Co and Fe nanoparticles generated in the conversion reaction improved the electronic conductivity of the electrode. Despite the capacity decay of CFSe/C-500 over long-term cycles, all three samples exhibited good KIB performance, and CFSe/C-250 stood out as the best, delivering a capacity of 485 mAh g^{-1} after 200 cycles at 0.1 A g^{-1} and retaining 272 mAh g^{-1} at 2 A g^{-1}, as well as fully recovering the capacity at 0.5 A g^{-1} in the following cycles (Figures 7B and 7C). The authors ascribed the performance to several structural merits of the composites, including a large void space in the nanospheres to facilitate K^+ diffusion and accessibility, a conductive carbon frame to reinforce the structural stability during cycles, and restrained volume expansion of CFSe nanoparticles due to their confinement within small-sized pores. A general approach was reported to produce nanostructured binary selenides as NIB anodes, including Fe-Ni, Fe-Co, and Ni-Co

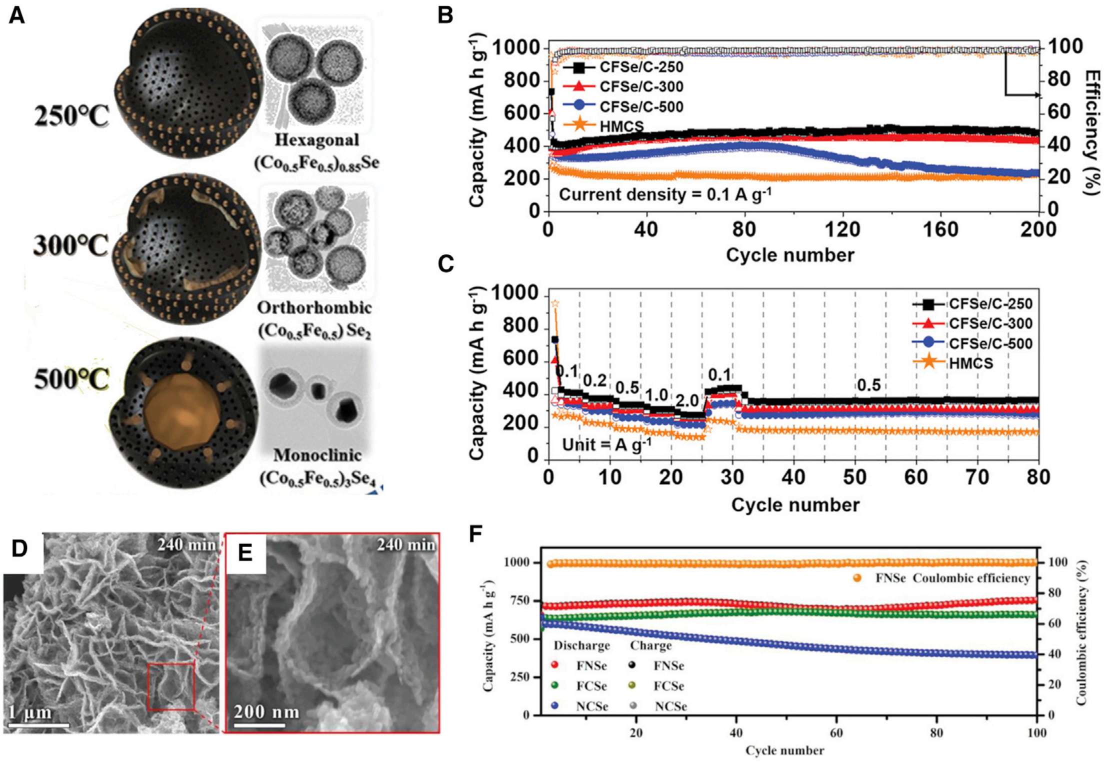

Figure 7. Engineering binary selenides for NIBs and KIBs

(A) Structural schematics and TEM images of CFSe/C at various selenization temperatures.

(B and C) Cycling performance (B) and rate capability (C) of CFSe/C composites in KIBs. Reproduced with permission.[50] Copyright 2020, Wiley-VCH.

(D and E) SEM images of FNSe.

(F) Cycling performance of FNSe, FCSe, and NCSe in NIBs. Reproduced with permission.[51] Copyright 2018, Wiley-VCH.

selenides (FNSe, FCSe, and NCSe).[51] The approach consisted of two steps, reduction of the mixed metal sulfate precursor solution and selenization in a gas phase, which resulted in a high yield of products. The time of the first step was optimized to obtain a 2D sheet-like structure that consisted of homogeneously distributed nanoparticles (Figures 7D and 7E). Phase transition of the binary selenides was studied for FNSe, showing a reversible conversion reaction during the initial sodiation or desodiation and the disappearance of FNSe peaks below 0.5 V. Therefore, the binary selenides were cycled in a voltage range of 0.5–3.0 V to avoid the conversion reaction at a lower voltage. Compared with NCSe, FNSe and FCSe exhibited impressive cyclability at high rates, delivering 755 and 660 mAh g^{-1} after 100 cycles at 1 A g^{-1} and 553 and 550 mAh g^{-1} after 2,600 cycles at 4 A g^{-1}, respectively (Figure 7F). Good rate capability was found in FNSe and FCSe as well, and they maintained the capacities of 427 and 466 mAh g^{-1}, respectively, at a rate as high as 20 A g^{-1}. In particular, the authors synthesized mono-metal selenides of Fe, Ni, and Co using the same approach as for the binary selenides but with a single metal precursor, and the three binary selenides outperformed their mono-metal counterparts in capacity, cycling stability, and rate capability, which was attributed by the authors to the better intrinsic conductivity and larger crystal structures of the binary selenides.

Discharge cutoff voltage has been shown to be important to the performance of binary MSs. Most studies chose 0.5 V as the cutoff voltage, as previously mentioned, to avoid a complete conversion reaction and the associated large volume change. Furthermore, studies of $Co_{1.5}Fe_{1.5}Se_4$ for KIBs[50] and $NiCo_2Se_4$ for NIBs[52] showed

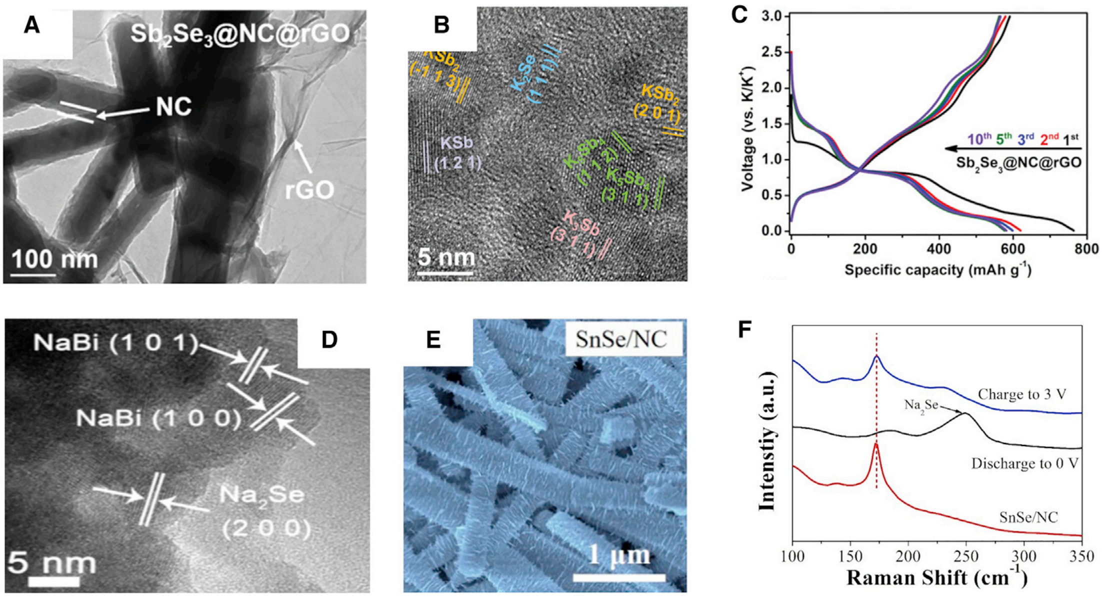

Figure 8. Alloy engineering in MSs for NIBs and KIBs
(A) TEM image of Sb_2Se_3@NC@rGO.
(B) HRTEM image of the Sb_2Se_3@NC@rGO electrode discharged to 0.01 V.
(C) Charge-discharge curves of Sb_2Se_3@NC@rGO in KIBs. Reproduced with permission.[56] Copyright 2020, Wiley-VCH.
(D) HRTEM image of the Bi_2Se_3/GNS electrode discharged to 0.5 V. Reproduced with permission.[54] Copyright 2018, American Chemical Society.
(E) SEM image of SnSe/NC nanobelts.
(F) Raman spectra of the SnSe/NC electrode at different discharge and charge states in NIBs. Reproduced with permission.[57] Copyright 2018, Elsevier.

that when initially discharging the binary MSs to 0.01 V, phase separation was observed in the subsequent charge process, resulting in the formation of $FeSe_2$/$CoSe_2$ and $CoSe_2$/NiSe in the respective studies. This could cause an increase in the resistance in the electrode matrices because of the lower intrinsic conductivity of the mono-metal selenides. Therefore, care needs to be taken when choosing a discharge cutoff voltage, and further material engineering should be sought to alleviate phase separation.

Alloy engineering

Most MSs discussed in the previous sections undergo a conversion reaction to store Na^+/K^+, in which MSs are reduced to metals and Na_xSe_y/K_xSe_y. Because elements such as Sn, Sb, and Bi can alloy with Na^+/K^+, their selenides (Sb_2Se_3,[53] Bi_2Se_3,[54] SnSe[55,64], and $SnSe_2$[65,66]) can store the ions by undergoing not only a conversion reaction but also a subsequent alloying reaction. As a result, this type of alloying engineering can greatly increase capacity by employing the alloying ability of the metals. Alloying reactions induce large volume expansion of selenides and can cause pulverization and unstable cyclability; hence, this type of selenide is spatially confined by carbon materials.

Wang et al.[56] reported a composite of Sb_2Se_3/N-doped carbon/reduced graphene oxide (Sb_2Se_3@NC@rGO), in which Sb_2Se_3 nanorods were directly encapsulated by a uniform amorphous NC layer (Figure 8A), and a few layers of rGO nanosheets tightly covered the NC layer, acting as a flexible shell. The lattice fringes of the composite after discharging to 0.01 V (Figure 8B) suggested that a mixture of K-Sb alloys was formed, including KSb_2, KSb, K_5Sb_4, and K_3Sb. Due to the coexistence of the conversion reaction of Sb_2Se_3 and the alloying reaction between Sb and K, as evidenced by the discharge plateaus at 0.8 and 0.2 V, respectively (Figure 8C), the composite delivered a high capacity of 580 mAh g^{-1} after 10 cycles and retained 450 mAh g^{-1} after 50 cycles. The authors compared the thicknesses of different control electrodes (Sb_2Se_3, Sb_2Se_3@NC, and Sb_2Se_3@rGO) after 8 cycles and found that the Sb_2Se_3@NC@rGO electrode had the smallest change in thickness, indicating that the electrode experienced the smallest change in volume and hence possibly the highest structural stability because of the confinement effect ensured by rGO. Li et al.[54] designed a composite of Bi_2Se_3 and graphene nanosheets (GNSs) through a selenization reaction, and the composite exhibited a curled morphology and wrinkled structure. When discharging the composite to 0.5 V in a NIB half-cell, NaBi and Na_2Se were formed and detected (Figure 8D), which suggested an alloying reaction occurred between Bi and Na. The Bi_2Se_3/GNS anode delivered capacities of 222 and 183 mAh g^{-1} at 2 and 10 A g^{-1} after 1,000 cycles, respectively. Ren et al.[57] applied alloy engineering to SnSe and synthesized SnSe nanoplates vertically grown on N-doped carbon nanobelts (SnSe/NC), forming a nanoribbon morphology with many nanosheets vertically on the surface (Figure 8E). The Raman shift to 249 cm^{-1} (Figure 8F) indicated that when the SnSe/NC anode was discharged to 0.01 V, Na_2Se and an amorphous Na_xSn alloy formed. The shift was recovered upon charging the anode to 3.0 V. The SnSe/NC anode showed a large capacity of 723 mA h g^{-1} at 25 mA g^{-1} after 50 cycles, benefiting from the alloying reaction, and 82% of the initial capacity remained after 200 cycles at 2 A g^{-1}, mainly because the Sn-C bonding can effectively prevent SnSe from accumulating during cycling to remain in the structure.

COMPOSITE ENGINEERING

Composites with carbons

Non-graphitic carbons form composites with selenides in various forms, such as a supporting matrix,[45,58] a coating layer,[59] and an encapsulation structure.[60–62] Nanostructured selenides are prone to agglomeration and form inactive clusters; hence, improving the dispersion of small-sized selenides on a carbon matrix is imperative. Liu et al.[63] prepared $Co_{0.85}Se$ quantum dots ($Co_{0.85}Se$-QDs) encapsulated in a mesoporous polyhedral carbon matrix via one-step hydrothermal selenization (Figure 9A), in which the Co precursor transformed to $Co_{0.85}Se$-QDs and decomposed to mesoporous and hollow carbon polyhedra (Figure 9B). The polyhedra acted as a carbon matrix to host the QDs and restrain their agglomeration when storing K^+ and at the same time contributed as a three-dimensional (3D) hierarchical network that can facilitate electron transfer and enhance the structural integrity of the composite. The composite as a KIB anode delivered a capacity of 402 mAh g^{-1} at 50 mA g^{-1} after 100 cycles (Figure 9C) and retained 228 mAh g^{-1} at 1 A g^{-1} after 500 cycles. Lu et al.[67] reported a hierarchical hybrid yolk-shell structure of carbon-coated $FeSe_2$ microcapsules ($FeSe_2$@C-3 MCs) (Figure 9D) and demonstrated that the composite could be a universal conversion-type anode material for LIBs, NIBs, and KIBs. The composite exhibited a very high ICE of 92.8% with a cutoff voltage of 0.5 V in NIBs and impressive rate capability and cyclability, retaining 410 mAh g^{-1} at 1 A g^{-1} over 1,000 cycles and 371.7 mAh g^{-1} at 10 A g^{-1} over 1,500 cycles (Figure 9E). When reducing the cutoff voltage to 0.01 V in KIBs (Figure 9F), the composite delivered 227.7 mAh g^{-1} at 0.1 A g^{-1} and 141.8 mAh g^{-1} at 2 A g^{-1}. The authors ascribed the performance to the multiple benefits derived from the hierarchical hybrid structure. The interconnected carbon shell can improve the mechanical strength of the electrode and accelerate ion and electron migration, as well as restraining the internal electroactive $FeSe_2$ nanoparticles and avoiding their pulverization. More importantly, the yolk-shell structure can provide a sufficient inner void to

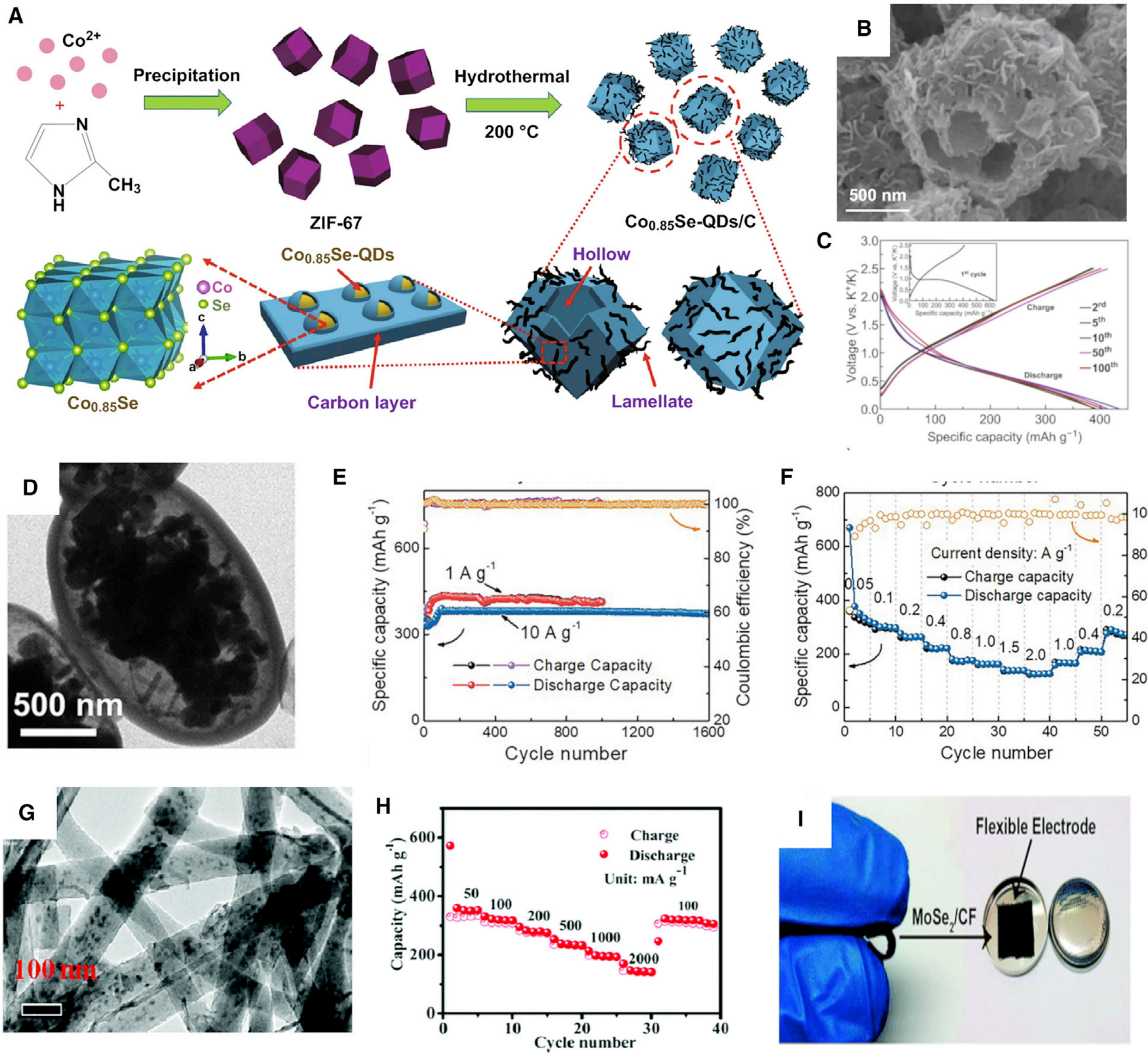

Figure 9. Engineering MS/non-graphitic carbon composites for NIBs and KIBs

(A) Schematics of the synthesis process of $Co_{0.85}Se$-QDs/C.

(B) SEM image of $Co_{0.85}Se$-QDs/C-20.

(C) Charge-discharge curves of $Co_{0.85}Se$-QDs/C-20 at different cycles in KIBs (inset is the curves of the first cycle). Reproduced with permission.[63] Copyright 2019, Springer.

(D–F) TEM image (D), cycling performance in NIBs (E), and rate capability in KIBs (F) of $FeSe_2$@C-3 MCs. Reproduced with permission.[67] Copyright 2021, Wiley-VCH.

(G and H) TEM image (G) and rate capability (H) of the $VSe_{1.5}$/CNF composite in KIBs. Reproduced with permission.[68] Copyright 2019, Royal Society of Chemistry.

ensure electrolyte infiltration and mobilize the nanoparticles, which was demonstrated by the yolk-shell-structured electrode outperforming the core-shell-structured counterpart (no inner void). Besides 3D spheric encapsulation, one-dimensional (1D) cable-like encapsulation has been reported for MS/carbon composites, which shares the benefits of increasing electronic conductivity, providing network for charge migration, and enhancing the structural integrity of electrodes, as well as avoiding the agglomeration of selenides. A $VSe_{1.5}$/carbon nanofiber ($VSe_{1.5}$/CNF) composite was synthesized through an electrospinning method followed by selenization.[68] $VSe_{1.5}$/CNF exhibited a fibrous structure, and $VSe_{1.5}$ nanoparticles were well distributed over the entire CNF (Figure 9G). The results showed that the composite can enable rapid and durable storage for both Na^+ and K^+. As an anode for NIBs, $VSe_{1.5}$/CNF delivered a high capacity of 668 mAh g^{-1} at 50 mA g^{-1} and retained 265 mAh g^{-1} at 2 A g^{-1} after 6,000 cycles. As an anode in KIBs, $VSe_{1.5}$/CNF delivered 313 and 177 mAh g^{-1} at 0.1 and 1 A g^{-1}, respectively (Figure 9H). Electrospinning has been used to fabricate various MS/CNF composites, including $CoSe_2$,[69] $MoSe_2$,[70] and Fe_3Se_4.[107] The $CoSe_2$/CNF composite delivered an impressive rate capability of 224 mAh g^{-1} at 15 A g^{-1} in NIBs.[69] The encapsulated structure was kept well intact after the composite was cycled at 2 A g^{-1} for 1,000 cycles. Apart from the previously discussed benefits, using carbon cloth (an array of CNFs) as a substrate enables the direct growth of MSs on the substrate, realizing flexible and self-supported electrodes (Figure 9I).[71,72] This type of electrode eliminates the use of conductive additive and organic binder, which reduces electrochemically inactive weight and increases the gravimetric capacity of the electrodes.

Graphitic carbons form composites with MSs in forms similar to those of non-graphitic carbons. Commonly used graphitic carbons include few-layered graphene/rGO[73–78] and CNTs.[79–81] Incorporating graphitic carbons with MSs brings the general benefits discussed in the last paragraph, but there are unique benefits because of the physical and chemical features of graphitic carbons; hence, literature that reported such features are discussed next.

Random orientation and distribution of MSs and carbons in the composites can weaken interface contact and insufficiently reduce charge transfer resistance between the two components. Hence, intimate contact and interface coupling between them are desirable to enable fast charge transfer kinetics and great structural stability. Zhao et al.[77] reported the controlled growth of oriented $MoSe_2$ nanosheets on graphene through Mo-C bonding enabled by a surfactant-directed hydrothermal reaction. The key to ensure strong Mo-C chemical bonding was the use of the surfactant hexadecyltrimethyl ammonium bromide (CTAB) that tuned the surface charge of graphene oxide (GO) by the interaction between its long-chain alkyl group and the GO basal plane and exposed positively charged CTA^+ to attract $MoO_4{}^{2-}$, directing the nucleation and oriented growth of $MoSe_2$ (Figure 10A). The DFT calculations (Figure 10B) revealed that charge redistributions mainly occurred at the Mo-C interface region, and the accumulated charge in the interface suggested chemically favorable Mo-C bonding. In addition, the oriented $MoSe_2$ growth can create enough open space between neighboring nanosheets to accommodate the volume change during Na^+ insertion/extraction. The synergistic effect of the strong Mo-C bonding and oriented $MoSe_2$ growth resulted in fast charge transfer kinetics, realizing a rate capability of 324 mAh g^{-1} at 3.2 A g^{-1} in NIBs (Figure 10C). The capacity was retained by 87% at the same current density even though the mass loading increased to 4.8 mg cm^{-2}. Surface functionalization of CNTs is a versatile strategy to alter the surface properties of CNTs and the growth and structure of electroactive materials in composites. Choi and Kang[79] took the advantage of acid-treated CNTs with oxygen functional groups to simultaneously achieve high dispersibility of CNTs and binding of CNTs with hydrophobic polystyrene (PS) nanobeads in a water-based spraying solution. Using a spray pyrolysis process with the spraying solution containing acid-treated CNTs, PS nanobeads, and the Mo precursor, the authors obtained porous structured CNT balls embedded with fullerene-like $MoSe_2$ nanocrystals (F-$MoSe_2$/CNT), and the uniformly distributed nanovoids in the balls were realized by the deposition of the well-dispersed PS nanobeads within CNTs (Figures 10D and 10E). The F-$MoSe_2$/CNT composite as a NIB anode exhibited an ICE of

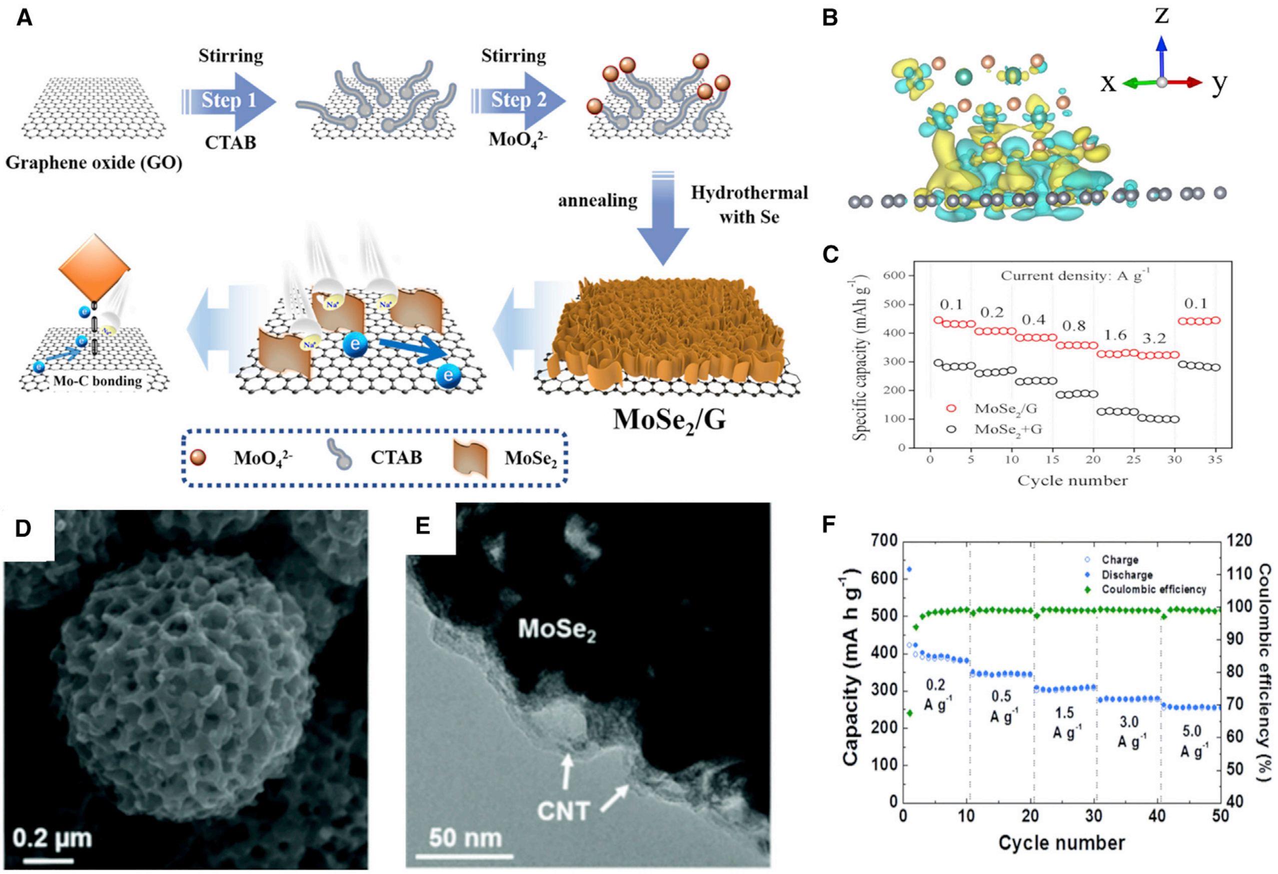

Figure 10. Engineering MS/graphitic carbon composites for NIBs and KIBs

(A) Schematics of the controlled growth of oriented MoSe$_2$ nanosheets on graphene through Mo-C bonding.

(B) Side view of the charge density difference of the MoSe$_2$/G heterostructure (the yellow/green cloud represents the negative/positive charge differences).

(C) Rate capability of the MoSe$_2$/G composite and a mixture of MoSe$_2$ and graphene in NIBs. Reproduced with permission.[77] Copyright 2018, Elsevier.

(D–F) SEM image (D), TEM image (E), and rate capability (F) of F-MoSe$_2$/CNT in NIBs. Reproduced with permission.[79] Copyright 2016, Royal Society of Chemistry.

75%, a capacity of 296 mAh g^{-1} at 1 A g^{-1} over 250 cycles, and a rate capability of 255 mAh g^{-1} at 5 A g^{-1} (Figure 10F), which were was ascribed to the synergetic combination of the nanovoids in the composite and the flexibility of CNTs. A composite of MoSe$_2$ nanosheet arrays grown on multi-walled CNTs was also synthesized by taking advantage of the surface functionalization of CNTs.[80]

Ternary composites consisting of a MS, a graphitic carbon, and a non-graphitic carbon have been reported in the literature.[82–84,86,116] In such a system, the MS was often coated with a layer of disordered carbon or encapsulated in CNFs, and the MS/non-graphitic carbon combination was embedded in graphitic carbon layers such as rGO and graphene. Although the synthesis of ternary composites might need multiple steps and extra care to manipulate the configuration, ternary composites benefit from the coexistence of graphitic and non-graphitic carbons, and the benefits can simultaneously take effect at short- and long-range scales in the composite matrix.

Composites with doped carbons

Heteroatom doping can tailor the electronic structure of carbons, induce defects to their structures, and hence enhance the interfacial ion adsorption and improve the

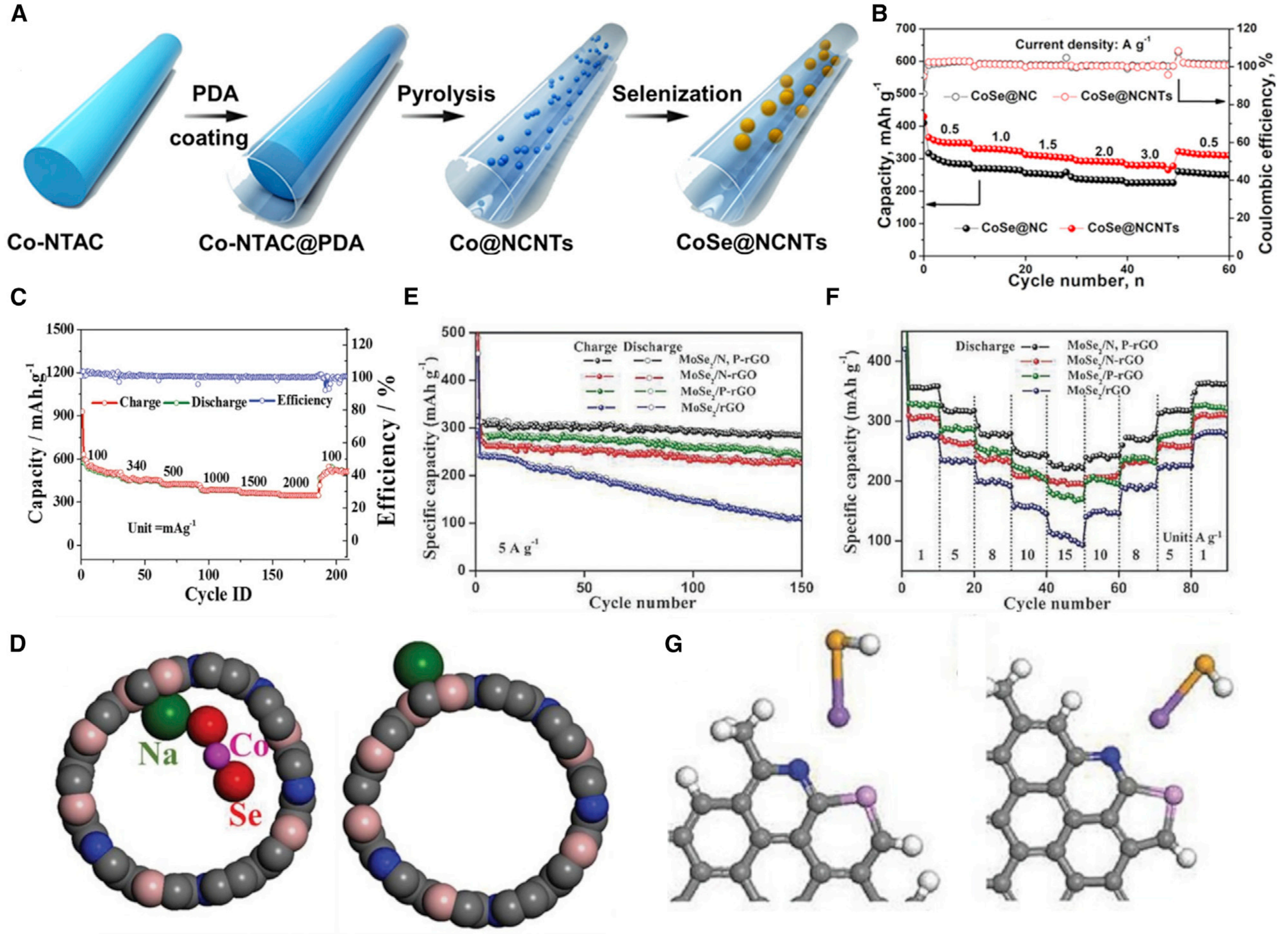

Figure 11. Engineering MS/doped carbon composites for NIBs and KIBs

(A) Schematics of the synthesis of CoSe@NCNTs.

(B) Rate capability of CoSe@NC and CoSe@NCNTs in KIBs. Reproduced with permission.[89] Copyright 2021, American Chemical Society.

(C) Rate capability of $CoSe_2$@BCN-750 nanotubes in NIBs.

(D) Schematic structures of Na-adsorbed $CoSe_2$@BCN nanotubes (left) and Na-adsorbed BCN nanotubes (right). Reproduced with permission.[92] Copyright 2019, Wiley-VCH.

(E and F) Cycling performance (E) and rate capability (F) of $MoSe_2$/N,P-rGO, $MoSe_2$/N-rGO, and $MoSe_2$/P-rGO electrodes in NIBs.

(G) Relaxed configurations of NaSeH interact with N,P-co-doped graphene (left: pyrrolic N; right: pyridinic N). Gray, white, blue, pink, violet, and brown spheres represent C, H, N, P, Na, and Se atoms, respectively. Reproduced with permission.[91] Copyright 2017, Wiley-VCH.

conductivity of carbons. This in turn can enhance the electrochemical performance of MS/doped carbon composites. Until now, most doped carbons in the MS composites have been N-doped carbon in the fields of NIBs and KIBs, which presumably results from the availability of a range of N-containing precursors that can be carbonized into N-doped carbon, such as $MoSe_2$/NPr composites,[87] VG/$MoSe_2$/N-C sandwiched core-shell arrays,[88] and $Fe_{0.8}CoSe$/N-C hollow nanospheres.[117] For instance, Liu et al.[89] synthesized CoSe nanoparticles confined in N-doped carbon nanotubes (CoSe@NCNTs), through which cobalt-nitrilotriacetic acid chelate (Co-NTAC) nanowires were first synthesized and coated with PDA to form a Co-NTAC@PDA core-shell structure that was further converted to CoSe@NCNTs after carbonization and selenization (Figure 11A). Both nitrilotriacetic acid and PDA contained N, and they both contributed to the formation of NCNTs. The composite exhibited a high ICE (95%), great capacity (435 mAg h^{-1} at 0.1 A g^{-1}), and stability (282 mAh g^{-1} at 2

A g^{-1} after 500 cycles) as a KIB anode (Figure 11B). There has been one study of a few-layered $MoSe_2$/P-doped graphene composite,[90] in which P doping can reduce the energy barrier of Na^+ diffusion and suppress the formation of Na clustering on graphene by increasing the binding energy on P-doped graphene.

Compared with the MS composites with mono-heteroatom-doped carbons, composites with co-heteroatom-doped carbons have rarely been investigated.[87,91,92,118] The dopants not only individually alter the electronic state and defective structure of carbons but also interact with each other and collectively affect the electron activation of C around them, further affecting the battery performance of the MS/codoped carbon composites. Tabassum et al.[92] demonstrated that B- and N-co-doped carbon (BCN) tubes enabled excellent Na^+ storage performance of $CoSe_2$ nanobuds ($CoSe_2$@BCN). The composite obtained at the optimized temperature (750°C) exhibited 386 and 338 mAh g^{-1} at 1 and 2 A g^{-1}, respectively (Figure 11C) and long-term stability of 96% capacity retention at 8 A g^{-1} over 4,000 cycles. Theoretical calculations (Figure 11D) revealed that the most stable Na adsorption sites on $CoSe_2$@BCN yielded adsorption energies of −2.83 and −2.23 eV. Among the Na adsorption sites on pristine BCN, including B-top, C-top, and the B-C/C-C/C-N bridge, the most stable sites yielded the adsorption energy of −2.10 eV, which was comparable to $CoSe_2$@BCN. In addition, both Na-adsorbed BCN and $CoSe_2$@BCN showed a metallic character, which contributed to improving the charge transfer in the composite. $MoSe_2$ grown on N- and P-co-doped carbon nanosheets ($MoSe_2$/N,P-rGO) showed excellent NIB performance by delivering 378 mAg^{-1} at 0.5 A g^{-1} after 1,000 cycles and retaining 55% capacity at 15 A g^{-1}.[91] Interestingly, the control samples $MoSe_2$/N-rGO, $MoSe_2$/P-rGO, and $MoSe_2$/rGO were outperformed by $MoSe_2$/N,P-rGO (Figures 11E and 11F). This indicated the synergistic effect of N and P codoping compared with N or P doping. The authors compared the binding strength of the terminal Na^+ of NaSeH (used to model the Na-Se end of the sodium polyselenide intermediate discharge product) on various doped forms of rGO. N doping significantly increased the binding energies on pyridinic N (0.94 eV) and pyrrolic N (1.22 eV) at the edge of rGO. Although P doping was unable to increase binding energy, both pyridinic and pyrrolic N could stay near P, bridging the dual coordination with NaSeH; as a result, the binding energy increased to 1.08 eV for pyridinic N/pyridinic P and 1.22 eV for pyridinic N/pyrrolic P (Figure 11G). The strong interaction between active species and co-doped carbons was responsible for the enhanced performance of $MoSe_2$/N,P-rGO over $MoSe_2$/N-rGO and $MoSe_2$/P-rGO. In addition, it was reported that N and S codoping can provide rich active sites and defects in carbons for Na^+ and K^+ adsorption and accelerate a surface/near-surface reaction with great pseudocapacitive effect.[118] As a result, the MS composite encapsulated in N- and S-co-doped hollow carbon nanospheres and interconnected rGO nanosheets exhibited a reversible capacity at a high current density in both NIBs (311 mAh g^{-1} at 10 A g^{-1}) and KIBs (310 mAh g^{-1} at 5 A g^{-1}).

Composites with compounds

Large volume expansion due to conversion reactions upon sodiation and potassiation can cause anisotropic swelling and anomalous structural deformation of MSs, resulting in electrode instability and inferior Na/K storage performance. It has been discussed in the previous sections that engineering MS composites with carbons, particularly with a hierarchical structure, has proven to be an effective strategy to tackle the issue. An external carbon layer can accommodate the structural deformation of MSs and form a heterointerface with MSs to boost ion capture and storage, as well as facilitate ion diffusion. However, the mechanical stress intensification

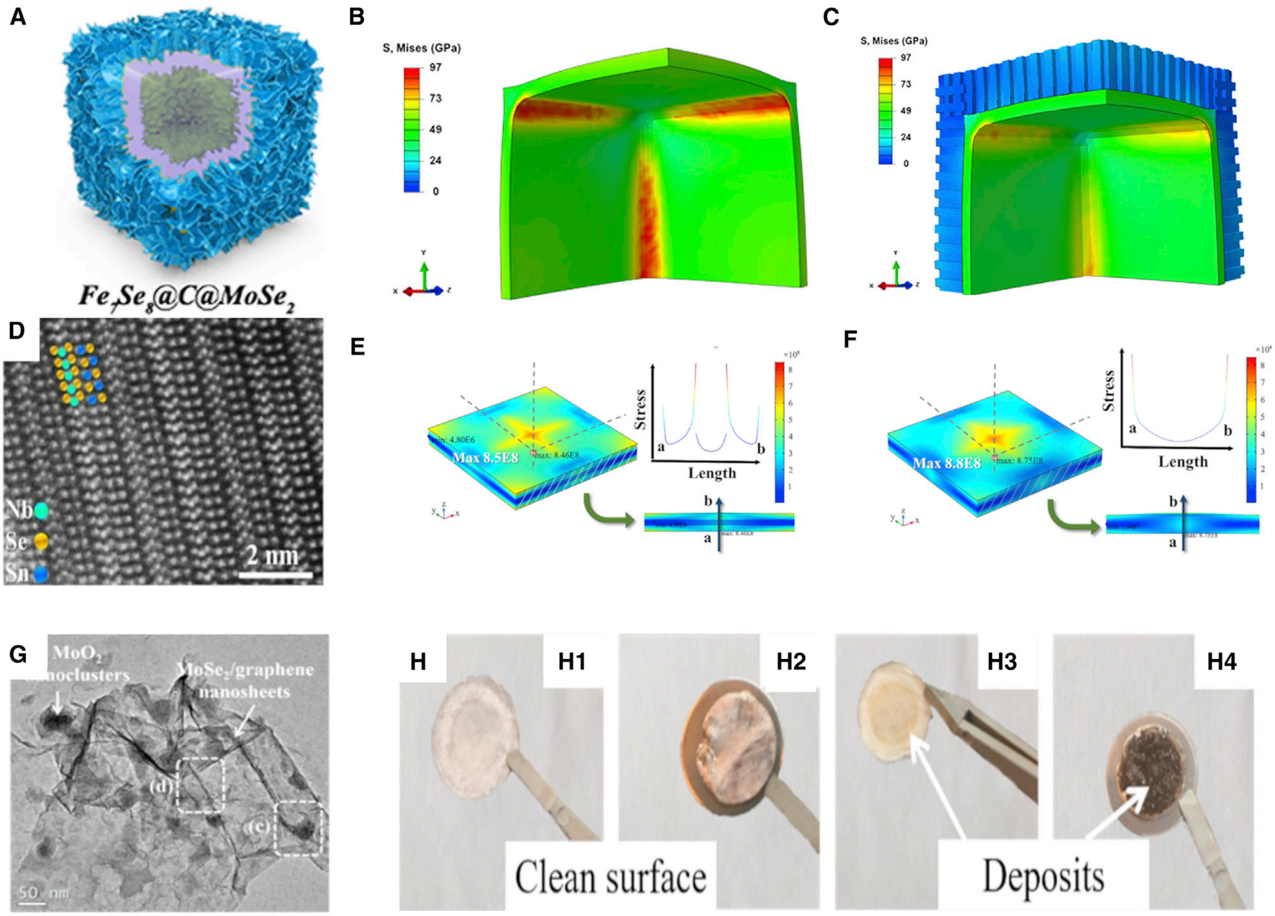

Figure 12. Engineering MS/compound composites for NIBs and KIBs

(A) Schematics of the Fe_7Se8@C@MoSe$_2$ composite.

(B and C) FE simulation comparing the strain and stress distributions of $Fe_7Se_8@C$ (B) and $Fe_7Se_8@C@MoSe_2$ (C) after sodiation. Reproduced with permission.[93] Copyright 2020, Elsevier.

(D) High-angle annular dark-field scanning transmission electron microscopy (HAADF-STEM) image of $(SnSe)_{1.16}NbSe_2$.

(E and F) 3D sectional and linear distributions of the external applied vertical Von-Mise stress on the $(SnSe)_{1.16}NbSe_2$ (E) and SnSe (F) structural units. Reproduced with permission.[119] Copyright 2021, Elsevier.

(G) TEM image of $MoO_2/MoSe_2$-graphene heterostructures.

(H) Photographs of the separators (H1 and H3) and sodium counter electrodes (H2 and H4) from dissembled cells (H1 and H2: $MoO_2/MoSe_2$-graphene; H3 and H4: $MoSe_2$-graphene) in NIBs. Reproduced with permission.[94] Copyright 2018, Elsevier.

caused by the large volume expansion of MSs has rarely been investigated when engineering composites with carbons. In this regard, a stress-release strategy was proposed by engineering composites with a compound that acts as a buffer layer to accommodate ion insertion-induced fracture from a mechanical standpoint. Chen et al.[93] demonstrated this strategy by growing $MoSe_2$ nanosheets onto the surface of a yolk-shell $Fe_7Se_8@C$ composite (Figure 12A). The authors performed finite element (FE) analysis to support that the $MoSe_2$ layer can reduce the risk of fracture in the carbon shell layer.[93] Assuming a constant and uniform expansion coefficient throughout the yolk-shell-structured $Fe_7Se_8@C$, after the initial expansion of the Fe_7Se_8 yolk within the void space upon sodiation, the contact with the carbon shell induced severe stress concentration along the edge of the cubic carbon shell, causing the highest strain of 37% and the fracture of the brittle carbon shell because of the in-plane tensile stress (63 GPa) in the middle cross-section (Figure 12B). With the $MoSe_2$ layer, a similar volume expansion level resulted in a more uniform stress distribution in the carbon shell, and the in-plane tensile stress in the shell was lowered to below 40 GPa (Figure 12C). Compared with Fe_7Se_8@C, Fe_7Se_8@C@$MoSe_2$ exhibited greatly improved performance, delivering high storage capacity (473.3 mAh g^{-1} at 0.1 A g^{-1}), great rate capability (274.5 mAh g^{-1} at 5 A g^{-1}), and cycling stability (87.1% capacity retention after 600 cycles at 1 A g^{-1}). Alternatively, misfit 2D layered MSs were reported to address the issue of mechanical stress to store K^+.[119] Misfit layered $(SnSe)_{1.16}NbSe_2$ had a unique sandwich structure that combined the merits of the two subunits (Figure 12D): $NbSe_2$ as a rigid unit providing excellent structure stability and a conductive framework and SnSe as a soft unit providing high reactivity and capacity. The FE analysis showed that the $(SnSe)_{1.16}NbSe_2$ sandwich structure can restrain the expansion of SnSe and avoid structural pulverization due to high Young's modulus of $NbSe_2$. Compared with SnSe, the external Von-Mise stress on the surface of the composite was more even and the peak value was smaller. The stress distribution curve of the longitudinal section (Figures 12E and 12F) demonstrated that the compression of SnSe could be shared by the top and bottom $NbSe_2$ layers in the sandwich structure.

Another issue of employing MSs in NIBs and KIBs is the formation of irreversible Na/K polyselenide and selenide species and the consequent shuttle effect that causes the loss of the MS phase and rapid capacity degradation. Instead of using carbons to constrain the polyselenide and selenide species during electrochemical reactions, compounds can be used for the same purpose by adsorbing the species. MoO_2 nanoclusters were anchored on the interface between $MoSe_2$ and graphene (Figure 12G) and acted as a heteroprotrusion to adsorb Na polyselenide species.[94] After the initial cycle of MoO_2/$MoSe_2$-graphene, a clean surface of the separator and Na disc can be seen without obvious deposits (Figures 12H1 and 12H2), whereas deposits were observed in the case of $MoSe_2$-graphene (Figures 12H3 and 12H4), indicating that the polyselenide species could be effectively trapped by the nanoscale heterojunction between MoO_2 and $MoSe_2$-graphene. Besides the phase recovery of $MoSe_2$, MoO_2 nanoclusters were dispersed and anchored on the 2D nanosheets, which prevented restacking of $MoSe_2$ layers during the reactions. The critical roles of MoO_2 resulted in the lamellar microstructure of MoO_2/$MoSe_2$-graphene being well preserved after cycles.

Engineering MSs with other compounds gives rise to heterointerfaces between the two components. Such heterointerfaces could offer unique benefits that might not be achieved in the composites with carbons. Apart from the release of mechanical stress and the absorption of polyselenide species, lattice distortion and mismatch at the heterointerfaces of $SnSe_2$/ZnSe can create a large amount of crystal defects and accessible active sites for Na^+ at the phase boundaries, which can promote the reaction kinetics.[95] Clean and tight interfaces in the graphene/$ReSe_2$/Ti_3C_2 sandwiched composite enabled by chemical vapor deposition can improve surface K^+ adsorption and lower the K^+ diffusion energy barrier compared with the composite made via wet chemistry routes.[96] Adjusting the compositional ratio between two MSs can dramatically change the morphology of the composite, showing a profound effect on the electrochemical performance of storing K^+.[120] These results from limited studies of MS/compound composites clearly highlight the importance and necessity to further explore such composites for NIBs and KIBs.

Interface engineering with electrolytes

Electrolytes are an equally important component as electrode materials in a NIB or KIB cell because electrolytes can determine the properties (e.g., chemical composition, structure, and resulting stability) of the SEI layer formed on the surface of MSs,

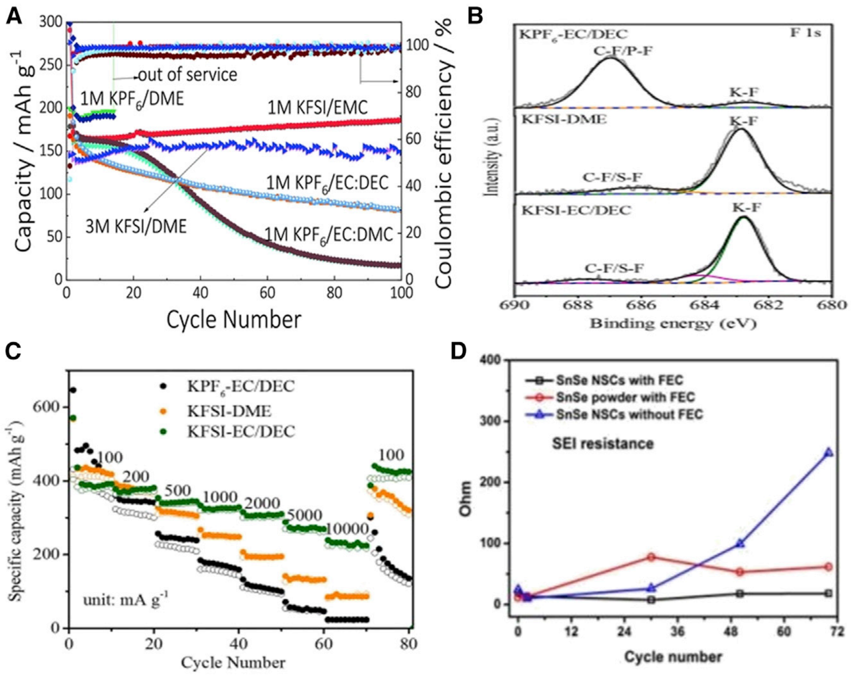

Figure 13. Interface engineering with electrolytes for MSs used in NIBs and KIBs

(A) Cycling performance of $MoSe_2$/NC in different electrolytes at 1 A g^{-1}. Reproduced with permission.[99] Copyright 2018, Wiley-VCH.

(B and C) F1s XPS spectra of cycled FeSe/C (B) and rate performance of FeSe/C (C) in various electrolytes. Reproduced with permission.[100] Copyright 2020, Elsevier.

(D) SEI layer resistance of SnSe with and without the FEC additive. Reproduced with permission.[101] Copyright 2016, Wiley-VCH.

i.e., the interface between MSs and electrolytes, which affects the cyclability, rate capability, and ICE of the cell. An unstable SEI layer often results in various complications: (1) irreversible side reactions between MSs and electrolytes can cause a low ICE during the formation of SEI when it is predominantly formed in the first cycle, (2) a SEI layer with poor mechanical stability can lead to a short cycle life of MSs, and (3) the continuous formation of a SEI layer because of continuous electrolyte decomposition can increase the thickness of the layer and deteriorate Na^+/K^+ diffusion, which damages the rate capability of MSs. Therefore, understanding the correlation between SEI formation and electrolytes is essential to engineering the MS/electrolyte interface.

One strategy to construct a stable SEI layer and obtain cycling stability of MSs is to tailor the combinations of electrolyte salt and solvent. Ge et al.[99] evaluated the durability of the $MoSe_2$/NC electrode using two salts, potassium bis(fluorosulfonyl)imide (KFSI) and potassium hexafluorophosphate (KPF_6), in solvents such as dimethyl ether (DME), ethyl methyl carbonate (EMC), ethylene carbonate:diethyl carbonate (EC:DEC), and ethylene carbonate:dimethyl carbonate (EC:DMC). The presence of KPF_6 in the electrolytes degraded cell durability irrespective of the solvents. Among the various electrolytes. 1 M KFSI/EMC exhibited 100-cycle stability at a high current density of 1 A g^{-1} (Figure 13A). Similar results were observed for FeSe/C when using KFSI as the salt in electrolytes,[100] in which the SEI layers formed in the electrolytes of KFSI/EC:DEC and KFSI/DME showed low content of the organic compound ROCOOK but were rich in inorganic compounds such as KF, $KHSO_4$, K_2SO_4, and K_2SO_3, which can be seen from the X-ray photoelectron spectroscopy (XPS) measurement of the cycled electrodes (Figure 13B). The existence of the inorganic compounds provided stability to the SEI layer; hence, cycling stability of FeSe/C was improved. In addition, KFSI increased the CE of FeSe/C because the FSI^- anion prevented the decomposition of solvent molecules. CE was initially ~75% in KFSI/EC:DEC and increased to ~100% by prolonging the cycles, but it was ~67% initially in KPF_6/EC:DEC and fluctuated between 80% and 90% during the following cycles. Furthermore, a thinner SEI layer (~5 nm) was found in the KFSI-based electrolyte compared with that in the KPF_6 counterpart (10–30 nm). This suggested less accumulation of the SEI layer derived by the continuous decomposition of the KFSI-based electrolyte and resulted in better K^+ diffusion and a higher D_K. As a result, the rate capability of FeSe/C in the KFSI/EC:DEC electrolyte was enhanced by ten-fold at a high current density of 10 A g^{-1} compared with the KPF_6/EC:DEC electrolyte (Figure 13C).

Another strategy to enhance the stability of the SEI layer is to use electrolyte additives. One of the most employed additives so far is fluoroethylene carbonate (FEC). It has a higher reduction potential than common solvent molecules and thus preferentially decomposes and forms a uniform and elastic SEI layer, suppressing the decomposition of electrolyte solvents. This is particularly crucial for MSs undergoing a dual process of conversion and alloying reactions and experiencing a huge volume change that could disrupt a previously formed SEI layer. Yuan et al.[101] used FEC as an electrolyte additive to enhance the NIB stability of N,S-co-doped carbon-coated SnSe (SnSe/NSC). The cell showed stable capacity in 100 cycles in the $NaPF_6$/EC:DEC electrolyte with the FEC additive but failed within 50 cycles without the additive. The authors attributed the results to the presence of FEC in the electrolyte, which provided low SEI resistance (Figure 13D), signifying control of the decomposition of electrolyte solvents and preventing side reactions of the electrolyte with SnSe/NSC. Besides the use of electrolyte additives, the stabilization of the SEI layer can be realized through the smart use of materials' surface bonding and their catalytic ability to catalyze SEI formation. This idea has been demonstrated for a sulfide anode recently[121] and is worth investigating for selenides. Fe-N-C and Fe-S-C bonds that were present in a FeS_2/N,S-codoped C composite acted as catalytic centers to promote the decomposition of the C-F bond in $NaSO_3CF_2$ (electrolyte salt) and the C-O bond in diglyme (electrolyte solvent), and they acted as crystal seeds to form ultra-thin (6.0 nm) and inorganic-rich SEI, resulting in a very high ICE of ~92% at 0.1 A g^{-1} and stable CE of ~100% at 3.0 A g^{-1} in 5,500 cycles.

CONCLUSIONS AND PERSPECTIVES

The last few years have seen rapidly increasing attention focused on using MSs as anode materials for NIBs and KIBs, and this review presents a timely summary of the recent progress on this topic. The review discusses various strategies for engineering MSs in response to the challenges that MSs are facing to store Na^+ and K^+. The discussed strategies are the most representative approaches that have been applied to MSs and by no means include all possible ones. Some strategies share common benefits, and our discussions aim to highlight the individual benefits of each strategy. Although remarkable progress has been made on MSs, we are still a long way from overcoming the obstacles to amplify the promise of MS anodes.

Unclear electrochemical mechanism of MSs in storing Na^+ and K^+

A great deal of efforts has been devoted to understanding the electrochemical mechanism of storing Na^+ and K^+ in MSs; however, the mechanism is still not fully understood and thus under debate, particularly regarding the differences between electrochemical Na and K systems, as well as the electrochemical reactivity of Se. This is reflected by the vastly different or even contradictory ion storage processes reported in the literature of MSs. It has been repeatedly observed that the end-discharge product A_xSe_y (A = Na or K) presents in a range of x/y ratios and consists of either a single ratio or more often a mixture of several ratios. These observations suggest that the conversion process from a MS to A_xSe_y deviates from an ideally single step of sodiation/potassiation, suggesting that it is inappropriate to treat the Na and K systems as empirically equal before investigating the conversion process in detail. Furthermore, understanding of the behavior of Se is far less available than that of the conversion process to A_xSe_y. It has been reported in a study of CuSe[97] that Se was found after the initial discharge in a KIB cell, but not in a NIB cell. Oppositely, the presence of Se was detected after the initial charge of $MoSe_2$, instead of the initial discharge, in both NIBs[91] and KIBs.[122] These results manifest the difference of applying MSs in the Na and K systems and highlight the necessity of investigating the change of Se^{2-}/Se. The formation of Se and its continuous presence in the electrode matrix could change the electrochemical process of storing the ions via the mechanism that is seen in Na/K-Se batteries. Therefore, in-depth investigation using advanced characterizations should be a route toward clear understanding of the Na^+/K^+ storage process and clarification of the results under debate. *In situ* characterizations are undoubtedly indispensable for reliably recording the ion storage process, and *ex situ* characterizations should be complementarily used to present accurate elucidation of the phase/microstructure/surface change of MSs during sodiation and potassiation.

The shuttle effect of polyselenides

The observation of A_xSe_y during and at the end of discharge clearly indicates the possibility of the shuttle effect of polyselenides, particularly high-order polyselenides, because they have a stronger tendency to dissolve in organic electrolytes compared with low-order polyselenides. The shuttle effect could result in low CE and rapid loss of active electrode materials, which has been repeatedly seen in studies of metal-S and metal-Se batteries. The formation of A_xSe_y and the subsequent shuttle effect form an evolving process and could be case specific, depending on a specific MS, so the process needs to be thoroughly investigated alongside the investigation of the electrochemical mechanism discussed in the last paragraph, preferentially using *in situ* characterizations due to the evolving nature of the process. Approaches to reduce the shuttle effect of polyselenides could be using carbons or compounds to constrain MSs, as previously discussed in the section composite engineering, and adding a secondary component in the MS composites, which has a stronger binding strength with polyselenides than electrolyte solvent molecules.[98] The component that has the most intimate contact with MSs during charge and discharge is SEI, and it should be given primary attention and studied when investigating the shuttle effect. This in turn leads to the need to study electrolyte formulation and the surface properties/modifications of MSs, with the aim of obtaining a stable SEI that could have a minimum possibility of A_xSe_y penetration.

The effect of electrolytes

The composition of electrolytes, including salts and solvents, is a crucial factor that could affect the electrochemical performance of MSs. This is particularly the case in KIBs because of the combination of the higher electrochemical activity of K^+ than Na^+ derived from the higher ionic conductivity of K^+ in electrolytes and the more sluggish kinetics and larger material volume change in KIBs. Organic KFSI as a salt has succeeded in various types of KIB electrode materials[123–126] because of a stable and protective SEI that is rich in KF, as opposed to the SEI that is formed by using KPF_6 and is deficient in KF. However, such an electrolyte salt has begun to emerge in the KIB research of MSs,[100] and there exist many unknow issues associated with how the salt affects the reaction kinetics and mechanism of KIB electrodes. Meanwhile, the role of electrolyte solvents cannot be ignored, because they could significantly downplay the advantages of certain types of salts[100] due to their involvement in the formation of SEI and interactions with the salts during SEI formation. In addition, the use of additives such as FEC has proved beneficial for alloying-based anodes but rather material specific for MSs in NIBs and KIBs; care needs to be taken when applying electrolyte additives. As a result, salts, solvents, and additives collectively affect the electrochemical performance, and the combination of them needs to be synergistically investigated. Besides organic electrolytes, ionic liquids (ILs) have started gaining attention in NIBs and KIBs because of their high ionic conductivity and wide electrochemically stable voltage window. These benefits have led to positive results prominently in the study of cathode materials, because a high operation voltage is highly desirable.[127,128] However, whether ILs could bring benefits to MSs remains to be seen, and little is known about the possible challenges that need to be addressed to gain the benefits. It is imperative to optimize the existing electrolyte formulas and formulate new molecules for electrolytes via new chemistries, with the aims of high Na^+/K^+ conductivity and CE, the ability to form stable SEI, and the inhibition of side reactions.

Scaling up and full-cell optimization

Through a survey of the research on MSs in NIBs and KIBs, one may find that the synthesis of MSs has been dominated by the hydro/solvothermal method, either to produce metal-containing precursors or to directly obtain MSs. In the case of former, a second step of gas-phase selenization is required. These synthetic procedures fall short of time efficiency and cost effectiveness, imposing limitations to scale up the production of MSs from a manufacturing point of view. Scalable synthesis methods are worth developing to bridge the gap between lab-scale demonstration and industry-level production. These methods should not be developed at the expense of precise control over the desirable phase, micro/nanostructure, and composition of MSs. From a practical point of view, pairing MSs with suitable cathodes to construct full cells should be kept in mind when investigating MSs in a half-cell configuration, which has not often been seen in the literature. Full-cell demonstration is important not only because it solidifies the promise of MSs but also because it aids in understanding the practical issues that would not be encountered in half-cells, including electrolyte compatibility, anode/cathode mass ratio, and operating voltage window. For instance, the high capacity of MS anodes does not necessarily contribute to an increase of full-cell capacity because of an increase of cathode mass to balance the charge. Studies of LIBs have shown that full-cell gravimetric capacity and energy density reach a saturated state for an anode capacity beyond 1,000 mAh g^{-1}[129] when the cathode capacity is 200 mAh g^{-1} or less. Currently, the best performing NIB and KIB cathodes deliver a capacity of 130–160 mAh g^{-1}, so when using a MS anode, a gain in full-cell capacity and energy density could be generated only if a higher cathode capacity would be available.[130] Thus, MS anodes should be carefully designed to deliver an optimized capacity in combination with the chosen cathode, electrolyte, and operation voltage window; hence, the contribution of MSs could be maximized.

Practical application of MSs

Although significant progress has been made to achieve high performance of MSs at a lab scale, a few aspects are worth investigating from an application-based point of view to facilitate the practical use of MSs in a commercialization setting:

(1) Active material loading: one of the most important figures of merit of batteries is capacity per mass of active material. It is known that electrodes that exhibit good battery performance with low active material loading may not be able to maintain their performance when active material loading is increased. This is an issue from the perspective of commercialization. Until now, the MS loading investigated in the NIB and KIB literature has been far below commercial requirement (5–20 mg cm^{-2});[131] hence, a performance study at high MS loading needs attention to understand the limiting factors of achieving low-material-loading performance. Such a study should primarily investigate factors such as active material utilization, electrolyte wettability and infiltration, and polyselenide dissolution. In addition, the proportion of inactive materials (binder and conducting carbon) in MS electrodes adds dead weight to battery cells. For instance, the coin-cell configuration at a lab scale uses inactive materials ranging from 20% to 40%, which is significantly higher than the commercial requirement (10%–12%). Because binder and conducting additive influence side reactions of MS electrodes, it is crucial to investigate how low content of inactive materials affects side reactions. Optimizing these factors in the fabrication process of electrodes to increase MS loading will ease the transfer of materials/technology to commercialization.

(2) Safety of active materials: safety is an inevitable factor that needs attention while looking into MSs from an application-based point of view. Besides electrolytes, the thermal reactivity of MSs in an electrolyte affects the safety of battery cells. Because of the exothermic reactions involved in electrochemically storing ions in MSs, the stability of the SEI layer could be weakened, leading to thermal runway. This is often overlooked in a coin-cell prototype of NIBs and KIBs and could be better investigated in a prototype of a cylinder or pouch cell that better fits with advanced characterizations such as X-ray tomography. Furthermore, the investigation should take into consideration of the type of electrolyte; as previously discussed in this review, the formation and composition of SEI layers are closely related to electrolytes and could be vastly different from one electrolyte to another.

(3) High-voltage cathodes: the potential range of storing Na^+/K^+ ions in MSs often exceeds 2 V versus Na^+/Na or K^+/K, which is higher than classic cathode materials such as graphite and can substantially reduce the voltage of NIB/KIB full cells. For instance, $MoSe_2$, which operates between 1 and 2 V versus Na^+/Na, was coupled with $Na_3V_2(PO_4)_3$ cathode and delivered an average voltage plateau at 1.65 V,[43] which significantly reduced the full-cell energy density. Hence, it is crucial to develop high-voltage cathode materials with an operating potential of >4 V. However, such high potential causes instability of electrolytes (which is more critical for KIBs than NIBs) and limits the complete utilization of redox reactions at the cathode. Even with an electrolyte that is stable at a high potential, irreversible oxygen evolution has been observed in layered transition metal oxide cathodes when operated beyond 4.5 V, which can destabilize the cathodes' structures and result in irreversible capacity. In addition, the evolved oxygen can accelerate the decomposition of electrolytes, which solidifies the significance of developing high-voltage NIB/KIB cathode materials. Utilization of oxygen redox activity at a high potential seems to be an approach worth trying, but care needs to be taken when controlling the oxidation/reduction level of the oxygen species in the layered oxide cathodes.

LIBs have immensely contributed to shaping the modern world, but battery technologies based on Earth's abundant elements are indispensable for sustainable energy storage; in this regard, NIBs and KIBs have begun to show promise as alternatives for LIBs. The substantial progress achieved to date from MSs and other families of electrode materials has undoubtedly solidified the promise that NIBs and KIBs hold. We hope this review can provide useful insights on understanding of electrochemical storage of Na^+ and K^+ for the battery research community and in a wider sense shed some light on material design for other research domains.

ACKNOWLEDGMENTS

Y.X. acknowledges support from the Engineering and Physical Sciences Research Council (grant EP/V000152/1).

AUTHOR CONTRIBUTIONS

Conceptualization, Y.L. and Y.X.; writing – original draft, Y.L. and A.P.V.K.S.; writing – review & editing, Y.L., A.P.V.K.S., Y.X., and R.W.; supervision and funding acquisition, Y.X.

DECLARATION OF INTERESTS

The authors declare no competing interests.

REFERENCES

1. Chen, J., Chua, D.H., and Lee, P.S. (2020). The Advances of Metal Sulfides and In Situ Characterization Methods beyond Li Ion Batteries: Sodium, Potassium, and Aluminum Ion Batteries. Small Methods *4*, 1900648.
2. Hwang, J.-Y., Myung, S.-T., and Sun, Y.-K. (2017). Sodium-ion batteries: present and future. Chem. Soc. Rev. *46*, 3529–3614.
3. Yabuuchi, N., Kubota, K., Dahbi, M., and Komaba, S. (2014). Research development on sodium-ion batteries. Chem. Rev. *114*, 11636–11682.
4. Kundu, D., Talaie, E., Duffort, V., and Nazar, L.F. (2015). The Emerging Chemistry of Sodium Ion Batteries for Electrochemical Energy Storage. Angew. Chem. Int. Ed. *54*, 3431–3448.
5. Hosaka, T., Kubota, K., Hameed, A.S., and Komaba, S. (2020). Research Development on K-Ion Batteries. Chem. Rev. *120*, 6358–6466.
6. Rajagopalan, R., Tang, Y., Ji, X., Jia, C., and Wang, H. (2020). Advancements and Challenges in Potassium Ion Batteries: A Comprehensive Review. Adv. Funct. Mater. *30*, 1909486.
7. Zhang, W., Liu, Y., and Guo, Z. (2019). Approaching high-performance potassium-ion batteries via advanced design strategies and engineering. Sci. Adv. *5*, eaav7412.
8. Hwang, J.Y., Myung, S.T., and Sun, Y.K. (2018). Recent Progress in Rechargeable Potassium Batteries. Adv. Funct. Mater. *28*, 1802938.
9. Vaalma, C., Buchholz, D., Weil, M., and Passerini, S. (2018). A cost and resource analysis of sodium-ion batteries. Nat. Rev. Mater. *3*, 18013.
10. Yan, Z., and Obrovac, M. (2020). Quantifying the cost effectiveness of non-aqueous potassium-ion batteries. J. Power Sources *464*, 228228.
11. P. Ge and M. Fouletier (1988). Electrochemical intercalation of sodium in graphite. Solid State Ion. *28*, 1172–1175.
12. Jache, B., and Adelhelm, P. (2014). Use of graphite as a highly reversible electrode with superior cycle life for sodium-ion batteries by making use of co-intercalation phenomena. Angew. Chem. Int. Ed. *53*, 10169–10173.
13. Kim, H., Hong, J., Yoon, G., Kim, H., Park, K.-Y., Park, M.-S., et al. (2015). Sodium intercalation chemistry in graphite. Energy Environ. Sci. *8*, 2963–2969.
14. Kim, H., Yoon, G., Lim, K., and Kang, K. (2016). A comparative study of graphite electrodes using the co-intercalation phenomenon for rechargeable Li, Na and K batteries. Chem. Commun. (Camb.) *52*, 12618–12621.
15. Kishore, B., Venkatesh, G., and Munichandraiah, N. (2016). $K_2Ti_4O_9$: A Promising Anode Material for Potassium Ion Batteries. J. Electrochem. Soc. *163*, A2551.
16. Huang, J., Yuan, D., Zhang, H., Cao, Y., Li, G., Yang, H., et al. (2013). Electrochemical sodium storage of TiO_2(B) nanotubes for sodium ion batteries. Rsc Adv. *3*, 12593–12597.
17. Liu, X., Jiang, X., Zeng, Z., Ai, X., Yang, H., Zhong, F., Xia, Y., and Cao, Y. (2018). High Capacity and Cycle-Stable Hard Carbon Anode for Nonflammable Sodium-Ion Batteries. ACS Appl. Mater. Interfaces *10*, 38141–38150.
18. Zhao, J., Zou, X., Zhu, Y., Xu, Y., and Wang, C. (2016). Electrochemical Intercalation of Potassium into Graphite. Adv. Funct. Mater. *26*, 8103–8110.
19. Imtiaz, S., Amiinu, I.S., Xu, Y., Kennedy, T., Blackman, C., and Ryan, K.M. (2021). Progress and perspectives on alloying-type anode materials for advanced potassium-ion batteries. Mater. Today. Published online March 20, 2021. https://doi.org/10.1016/j.mattod.2021.02.008.
20. Han, W., Chen, D., Li, Q., Liu, W., Chu, H., and Rui, X. (2019). Ultrafast flame growth of carbon nanotubes for high-rate sodium storage. J. Power Sources *439*, 227072.
21. Yu, Y., Cheng, X., Li, D., Wu, Y., and Xu, R. (2019). Bismuth nanospheres embedded in three-dimensional (3D) porous graphene frameworks as high performance anodes for sodium- and potassium-ion batteries. J. Mater. Chem. A Mater. Energy Sustain. *7*, 4913–4921.
22. Zhao, Y., Ren, X., Xing, Z., Zhu, D., Tian, W., Guan, C., et al. (2020). In Situ Formation of Hierarchical Bismuth Nanodots/Graphene Nanoarchitectures for Ultrahigh-Rate and Durable Potassium-Ion Storage. Small *16*, 1905789.
23. Zhou, J., Liu, Y., Zhang, S., Zhou, T., and Guo, Z. (2020). Metal chalcogenides for potassium storage. InfoMat *2*, 437–465.
24. Ali, Z., Zhang, T., Asif, M., Zhao, L., Yu, Y., and Hou, Y. (2020). Transition metal chalcogenide anodes for sodium storage. Mater. Today *35*, 131–167.
25. Su, H., Jaffer, S., and Yu, H. (2016). Transition metal oxides for sodium-ion batteries. Energy Storage Mater. *5*, 116–131.
26. Hu, X., Zhang, N., Shinde, N.M., Mane, R.S., Xia, Q., and Kim, K.H. (2020). Potassium-Ion Batteries: Materials and Applications (Wiley), pp. 313–336.
27. Lu, T., Dong, S., Zhang, C., Zhang, L., and Cui, G. (2017). Fabrication of transition metal selenides and their applications in energy storage. Coord. Chem. Rev. *332*, 75–99.
28. Huang, X., Xu, Q., Gao, W., Yang, T., Zhan, R., Deng, J., Guo, B., Tao, M., Liu, H., and Xu, M. (2019). Rechargeable K-Se batteries based on

metal-organic-frameworks-derived porous carbon matrix confined selenium as cathode materials. J. Colloid Interface Sci. *539*, 326–331.

29. Wang, T., Legut, D., Fan, Y., Qin, J., Li, X., and Zhang, Q. (2020). Building Fast Diffusion Channel by Constructing Metal Sulfide/Metal Selenide Heterostructures for High-Performance Sodium Ion Batteries Anode. Nano Lett. *20*, 6199–6205.

30. Wang, X., Kong, D., Huang, Z.X., Wang, Y., and Yang, H.Y. (2017). Nontopotactic Reaction in Highly Reversible Sodium Storage of Ultrathin Co$_9$Se$_8$/rGO Hybrid Nanosheets. Small *13*, 1603980.

31. Zhao, X., Zhao, Y., Huang, B., Cai, W., Sui, J., Yang, Z., et al. (2020). Regulating safety and energy release of energetic materials by manipulation of molybdenum disulfide phase. Chem. Eng. J. *382*, 123047.

32. Shi, Z.T., Kang, W., Xu, J., Sun, L.L., Wu, C., Wang, L., Yu, Y.Q., Yu, D.Y., Zhang, W., and Lee, C.S. (2015). In Situ Carbon-Doped Mo(Se0.85 S0.15)2 Hierarchical Nanotubes as Stable Anodes for High-Performance Sodium-Ion Batteries. Small *11*, 5667–5674.

33. He, H., Huang, D., Gan, Q., Hao, J., Liu, S., Wu, Z., Pang, W.K., Johannessen, B., Tang, Y., Luo, J.-L., et al. (2019). Anion Vacancies Regulating Endows MoSSe with Fast and Stable Potassium Ion Storage. ACS Nano *13*, 11843–11852.

34. Li, B., Liu, Y., Li, Y., Jiao, S., Zeng, S., Shi, L., and Zhang, G. (2020). Dual-Functional Template-Directed Synthesis of MoSe$_2$/Carbon Hybrid Nanotubes with Highly Disordered Layer Structures as Efficient Alkali-Ion Storage Anodes beyond Lithium. ACS Appl. Mater. Interfaces *12*, 2390–2399.

35. Ge, P., Li, S., Xu, L., Zou, K., Gao, X., Cao, X., et al. (2019). Hierarchical Hollow-Microsphere Metal–Selenide@Carbon Composites with Rational Surface Engineering for Advanced Sodium Storage. Adv. Energy Mater. *9*, 1803035.

36. Zhang, J., Kang, W., Jiang, M., You, Y., Cao, Y., Ng, T.-W., Yu, D.Y., Lee, C.-S., and Xu, J. (2017). Conversion of 1T-MoSe$_2$ to 2H-MoS$_{2x}$Se$_{2-2x}$ mesoporous nanospheres for superior sodium storage performance. Nanoscale *9*, 1484–1490.

37. Yang, C., Feng, J., Lv, F., Zhou, J., Lin, C., Wang, K., et al. (2018). Metallic Graphene-Like VSe$_2$ Ultrathin Nanosheets: Superior Potassium-Ion Storage and Their Working Mechanism. Adv. Mater. *30*, 1800036.

38. Yu, Q., Jiang, B., Hu, J., Lao, C.Y., Gao, Y., Li, P., et al. (2018). Metallic Octahedral CoSe$_2$ Threaded by N-Doped Carbon Nanotubes: A Flexible Framework for High-Performance Potassium-Ion Batteries. Adv. Sci. *5*, 1800782.

39. Huang, H., Cui, J., Liu, G., Bi, R., and Zhang, L. (2019). Carbon-Coated MoSe$_2$/MXene Hybrid Nanosheets for Superior Potassium Storage. ACS Nano *13*, 3448–3456.

40. Zheng, N., Jiang, G., Chen, X., Mao, J., Zhou, Y., and Li, Y. (2019). Rational design of a tubular, interlayer expanded MoS$_2$–N/O doped carbon composite for excellent potassium-ion storage. J. Mater. Chem. A Mater. Energy Sustain. *7*, 9305–9315.

41. Zheng, F., Zhong, W., Deng, Q., Pan, Q., Ou, X., Liu, Y., et al. (2019). Three-dimensional (3D) flower-like MoSe$_2$/N-doped carbon composite as a long-life and high-rate anode material for sodium-ion batteries. Chem. Eng. J. *357*, 226–236.

42. Xiong, P., Ma, R., Sakai, N., Nurdiwijayanto, L., and Sasaki, T. (2018). Unilamellar Metallic MoS$_2$/Graphene Superlattice for Efficient Sodium Storage and Hydrogen Evolution. ACS Energy Lett. *3*, 997–1005.

43. Tang, Y., Zhao, Z., Wang, Y., Dong, Y., Liu, Y., Wang, X., and Qiu, J. (2016). Carbon-Stabilized Interlayer-Expanded Few-Layer MoSe$_2$ Nanosheets for Sodium Ion Batteries with Enhanced Rate Capability and Cycling Performance. ACS Appl. Mater. Interfaces *8*, 32324–32332.

44. Zhang, J., Wu, M., Liu, T., Kang, W., and Xu, J. (2017). Hierarchical nanotubes constructed from interlayer-expanded MoSe$_2$ nanosheets as a highly durable electrode for sodium storage. J. Mater. Chem. A Mater. Energy Sustain. *5*, 24859–24866.

45. Wang, W., Jiang, B., Qian, C., Lv, F., Feng, J., Zhou, J., et al. (2018). Pistachio-Shuck-Like MoSe$_2$/C Core/Shell Nanostructures for High-Performance Potassium-Ion Storage. Adv. Mater. *30*, 1801812.

46. Wei, X., Tang, C., An, Q., Yan, M., Wang, X., Hu, P., et al. (2017). FeSe$_2$ clusters with excellent cyclability and rate capability for sodium-ion batteries. Nano Res. *10*, 3202–3211.

47. Zhong, W., Ma, Q., Tang, W., Wu, Y., Gao, W., Yang, Q., et al. (2020). Construction of a bimetallic nickel–cobalt selenide pompon used as a superior anode material for high performance sodium storage. Inorg. Chem. Front. *7*, 1003–1011.

48. Xu, Z., Huang, Y., Chen, C., Ding, L., Zhu, Y., Zhang, Z., et al. (2020). MOF-derived hollow Co(Ni)Se$_2$/N-doped carbon composite material for preparation of sodium ion battery anode. Ceram. Int. *46*, 4532–4542.

49. Hou, B.H., Wang, Y.Y., Liu, D.S., Gu, Z.Y., Feng, X., Fan, H., et al. (2018). N-Doped Carbon-Coated Ni$_{1.8}$Co$_{1.2}$Se$_4$ Nanoaggregates Encapsulated in N-Doped Carbon Nanoboxes as Advanced Anode with Outstanding High-Rate and Low-Temperature Performance for Sodium-Ion Half/Full Batteries. Adv. Funct. Mater. *28*, 1805444.

50. Yang, S.H., Park, S.K., Park, G.D., Lee, J.H., and Kang, Y.C. (2020). Conversion Reaction Mechanism of Ultrafine Bimetallic Co-Fe Selenides Embedded in Hollow Mesoporous Carbon Nanospheres and Their Excellent K-Ion Storage Performance. Small *16*, 2002345.

51. Ali, Z., Asif, M., Huang, X., Tang, T., and Hou, Y. (2018). Hierarchically Porous Fe$_2$CoSe$_4$ Binary-Metal Selenide for Extraordinary Rate Performance and Durable Anode of Sodium-Ion Batteries. Adv. Mater. *30*, 1802745.

52. Qiu, L.-C., Wang, Q.-C., Yue, X.-Y., Qiu, Q.-Q., Li, X.-L., Chen, D., et al. (2020). NiCo$_2$Se$_4$ as an anode material for sodium-ion batteries. Electrochem. Commun. *112*, 106684.

53. Sheng, B., Wang, L., Huang, H., Yang, H., Xu, R., Wu, X., et al. (2020). Boosting Potassium Storage by Integration Advantageous of Defect Engineering and Spatial Confinement: A Case Study of Sb$_2$Se$_3$. Small *16*, 2005272.

54. Li, D., Zhou, J., Chen, X., and Song, H. (2018). Graphene-Loaded Bi$_2$Se$_3$: A Conversion-Alloying-type Anode Material for Ultrafast Gravimetric and Volumetric Na Storage. ACS Appl. Mater. Interfaces *10*, 30379–30387.

55. Zhao, W., Ma, X., Li, Y., Wang, G., and Long, X. (2020). Achieving ultrastable cyclability and pseudocapacitive sodium storage in SnSe quantum-dots sheathed in nitrogen doped carbon nanofibers. Appl. Surf. Sci. *504*, 144455.

56. Wang, S., Xiong, P., Guo, X., Zhang, J., Gao, X., Zhang, F., et al. (2020). A Stable Conversion and Alloying Anode for Potassium-Ion Batteries: A Combined Strategy of Encapsulation and Confinement. Adv. Funct. Mater. *30*, 2001588.

57. Ren, X., Wang, J., Zhu, D., Li, Q., Tian, W., Wang, L., et al. (2018). Sn-C bonding riveted SnSe nanoplates vertically grown on nitrogen-doped carbon nanobelts for high-performance sodium-ion battery anodes. Nano Energy *54*, 322–330.

58. Zhao, C., Shen, Z., Tu, F., and Hu, Z. (2020). Template directed hydrothermal synthesis of flowerlike NiSe$_x$/C composites as lithium/sodium ion battery anodes. J. Mater. Sci. *55*, 3495–3506.

59. Yang, X., and Zhang, Z. (2017). Carbon-coated vanadium selenide as anode for lithium-ion batteries and sodium-ion batteries with enhanced electrochemical performance. Mater. Lett. *189*, 152–155.

60. Su, Q., Cao, X., Kong, X., Wang, Y., Peng, C., Chen, J., et al. (2018). Carbon-encapsulated MoSe$_2$/C nanorods derived from organic-inorganic hybrid enabling superior lithium/sodium storage performances. Electrochim. Acta *292*, 339–346.

61. Yang, X., Zhang, Z., Fu, Y., and Li, Q. (2015). Porous hollow carbon spheres decorated with molybdenum diselenide nanosheets as anodes for highly reversible lithium and sodium storage. Nanoscale *7*, 10198–10203.

62. Ali, Z., Tang, T., Huang, X., Wang, Y., Asif, M., and Hou, Y. (2018). Cobalt selenide decorated carbon spheres for excellent cycling performance of sodium ion batteries. Energy Storage Mater. *13*, 19–28.

63. Liu, Z., Han, K., Li, P., Wang, W., He, D., Tan, Q., et al. (2019). Tuning Metallic Co$_{0.85}$Se Quantum Dots/Carbon Hollow Polyhedrons with Tertiary Hierarchical Structure for High-Performance Potassium Ion Batteries. Nano-Micro Lett. *11*, 1–14.

64. Lu, C., Li, Z., Xia, Z., Ci, H., Cai, J., Song, Y., et al. (2019). Confining MOF-derived SnSe nanoplatelets in nitrogen-doped graphene cages via direct CVD for durable sodium ion storage. Nano Res. *12*, 3051–3058.

65. Wang, T., Yang, K., Shi, J., Zhou, S., Mi, L., Li, H., et al. (2020). Simple synthesis of sandwich-

like $SnSe_2$/rGO as high initial coulombic efficiency and high stability anode for sodium-ion batteries. J. Energy Chem. *46*, 71–77.

66. Yang, K., Zhang, X., Song, K., Zhang, J., Liu, C., Mi, L., et al. (2020). Se–C bond and reversible SEI in facile synthesized $SnSe_2 \subset$ 3D carbon induced stable anode for sodium-ion batteries. Electrochim. Acta *337*, 135783.

67. Lu, S., Wu, H., Xu, S., Wang, Y., Zhao, J., Li, Y., et al. (2021). Iron Selenide Microcapsules as Universal Conversion-Typed Anodes for Alkali Metal-Ion Batteries. Small *17*, 2005745.

68. Xu, L., Xiong, P., Zeng, L., Fang, Y., Liu, R., Liu, J., Luo, F., Chen, Q., Wei, M., and Qian, Q. (2019). Electrospun $VSe_{1.5}$/CNF composite with excellent performance for alkali metal ion batteries. Nanoscale *11*, 16308–16316.

69. Yin, H., Qu, H.-Q., Liu, Z., Jiang, R.-Z., Li, C., and Zhu, M.-Q. (2019). Long cycle life and high rate capability of three dimensional $CoSe_2$ grain-attached carbon nanofibers for flexible sodium-ion batteries. Nano Energy *58*, 715–723.

70. Yang, X., Zhang, Z., and Shi, X. (2016). Rational design of coaxial-cable $MoSe_2$/C: Towards high performance electrode materials for lithium-ion and sodium-ion batteries. J. Alloys Compd. *686*, 413–420.

71. Guo, H., Liu, G., Wang, M., Zhang, Y., Li, W., Chen, K., Liu, Y., Yue, M., and Wang, Y. (2020). In-Situ Fabrication of Bone-Like $CoSe_2$ Nano-Thorn Loaded on Porous Carbon Cloth as a Flexible Electrode for Na-Ion Storage. Chem. Asian J. *15*, 1493–1499.

72. Zhang, Y., Liu, Z., Zhao, H., and Du, Y. (2016). $MoSe_2$ nanosheets grown on carbon cloth with superior electrochemical performance as flexible electrode for sodium ion batteries. RSC Advances *6*, 1440–1444.

73. Choi, J.H., Park, S.K., and Kang, Y.C. (2019). A Salt-Templated Strategy toward Hollow Iron Selenides-Graphitic Carbon Composite Microspheres with Interconnected Multicavities as High-Performance Anode Materials for Sodium-Ion Batteries. Small *15*, 1803043.

74. Liu, Z., Zhang, Y., Zhao, H., Li, N., and Du, Y. (2017). Constructing monodispersed $MoSe_2$ anchored on graphene: a superior nanomaterial for sodium storage. Sci. China Mater. *60*, 167–177.

75. Zhang, Z., Fu, Y., Yang, X., Qu, Y., and Zhang, Z. (2015). Hierarchical $MoSe_2$ Nanosheets/Reduced Graphene Oxide Composites as Anodes for Lithium-Ion and Sodium-Ion Batteries with Enhanced Electrochemical Performance. ChemNanoMat *1*, 409–414.

76. Cho, J.S., Park, S.-K., Jeon, K.M., Piao, Y., and Kang, Y.C. (2018). Mesoporous reduced graphene oxide/WSe_2 composite particles for efficient sodium-ion batteries and hydrogen evolution reactions. Appl. Surf. Sci. *459*, 309–317.

77. Zhao, X., Cai, W., Yang, Y., Song, X., Neale, Z., Wang, H.-E., et al. (2018). $MoSe_2$ nanosheets perpendicularly grown on graphene with Mo–C bonding for sodium-ion capacitors. Nano Energy *47*, 224–234.

78. Liu, Y., and Wang, X. (2019). Reduced Graphene Oxides Decorated NiSe Nanoparticles as High Performance Electrodes for Na/Li Storage. Materials (Basel) *12*, 3709.

79. Choi, S.H., and Kang, Y.C. (2016). Fullerene-like MoSe2 nanoparticles-embedded CNT balls with excellent structural stability for highly reversible sodium-ion storage. Nanoscale *8*, 4209–4216.

80. Zhang, Z., Yang, X., Fu, Y., and Du, K. (2015). Ultrathin molybdenum diselenide nanosheets anchored on multi-walled carbon nanotubes as anode composites for high performance sodium-ion batteries. J. Power Sources *296*, 2–9.

81. Tang, C., Wei, X., Cai, X., An, Q., Hu, P., Sheng, J., Zhu, J., Chou, S., Wu, L., and Mai, L. (2018). ZnSe Microsphere/Multiwalled Carbon Nanotube Composites as High-Rate and Long-Life Anodes for Sodium-Ion Batteries. ACS Appl. Mater. Interfaces *10*, 19626–19632.

82. Su, Q., Cao, X., Yu, T., Kong, X., Wang, Y., Chen, J., et al. (2019). Binding MoSe2 with dual protection carbon for high-performance sodium storage. J. Mater. Chem. A Mater. Energy Sustain. *7*, 22871–22878.

83. Cui, C., Zhou, G., Wei, W., Chen, L., Li, C., and Yue, J. (2017). Boosting sodium-ion storage performance of $MoSe_2$@C electrospinning nanofibers by embedding graphene nanosheets. J. Alloys Compd. *727*, 1280–1287.

84. Xie, D., Tang, W., Wang, Y., Xia, X., Zhong, Y., Zhou, D., et al. (2016). Facile fabrication of integrated three-dimensional C-$MoSe_2$/reduced graphene oxide composite with enhanced performance for sodium storage. Nano Res. *9*, 1618–1629.

85. Liao, Y., Chen, C., Yin, D., Cai, Y., He, R., and Zhang, M. (2019). Improved Na^+/K^+ Storage Properties of $ReSe_2$–Carbon Nanofibers Based on Graphene Modifications. Nano-Micro Lett. *11*, 22.

86. Park, G.D., Kim, J.H., Park, S.-K., and Kang, Y.C. (2017). $MoSe_2$ Embedded CNT-Reduced Graphene Oxide Composite Microsphere with Superior Sodium Ion Storage and Electrocatalytic Hydrogen Evolution Performances. ACS Appl. Mater. Interfaces *9*, 10673–10683.

87. Roy, A., Ghosh, A., Kumar, A., and Mitra, S. (2018). A high-performance sodium anode composed of few-layer $MoSe_2$ and N, P doped reduced graphene oxide composites. Inorg. Chem. Front. *5*, 2189–2197.

88. Xie, D., Xia, X., Zhong, Y., Wang, Y., Wang, D., Wang, X., et al. (2017). Exploring Advanced Sandwiched Arrays by Vertical Graphene and N-Doped Carbon for Enhanced Sodium Storage. Adv. Energy Mater. *7*, 1601804.

89. Liu, Y., Deng, Q., Li, Y., Li, Y., Zhong, W., Hu, J., Ji, X., Yang, C., Lin, Z., and Huang, K. (2021). CoSe@N-Doped Carbon Nanotubes as a Potassium-Ion Battery Anode with High Initial Coulombic Efficiency and Superior Capacity Retention. ACS Nano *15*, 1121–1132.

90. Xu, L., Ma, L., Ling, Y., Zhou, X., and Xu, X. (2018). $MoSe_2$/phosphorus-doped graphene nanocomposite: Synthesis and its electrochemical sodium-storage and catalytic performance. Colloids Surf. A Physicochem. Eng. Asp. *551*, 87–94.

91. Niu, F., Yang, J., Wang, N., Zhang, D., Fan, W., Yang, J., et al. (2017). $MoSe_2$-Covered N,P-Doped Carbon Nanosheets as a Long-Life and High-Rate Anode Material for Sodium-Ion Batteries. Adv. Funct. Mater. *27*, 1700522.

92. Tabassum, H., Zhi, C., Hussain, T., Qiu, T., Aftab, W., and Zou, R. (2019). Encapsulating Trogtalite $CoSe_2$ Nanobuds into BCN Nanotubes as High Storage Capacity Sodium Ion Battery Anodes. Adv. Energy Mater. *9*, 1901778.

93. Chen, S., Huang, S., Zhang, Y.-F., Fan, S., Yan, D., Shang, Y., et al. (2020). Constructing stress-release layer on Fe_7Se_8-based composite for highly stable sodium-storage. Nano Energy *69*, 104389.

94. Zhao, X., Wang, H.-E., Yang, Y., Neale, Z.G., Massé, R.C., Cao, J., et al. (2018). Reversible and fast Na-ion storage in MoO_2/$MoSe_2$ heterostructures for high energy-high power Na-ion capacitors. Energy Storage Mater. *12*, 241–251.

95. Liu, P., Han, J., Zhu, K., Dong, Z., and Jiao, L. (2020). Heterostructure $SnSe_2$/ZnSe@PDA Nanobox for Stable and Highly Efficient Sodium-Ion Storage. Adv. Energy Mater. *10*, 2000741.

96. Xia, Z., Chen, X., Ci, H., Fan, Z., Yi, Y., Yin, W., et al. (2021). Designing N-doped graphene/$ReSe_2$/Ti_3C_2 MXene heterostructure frameworks as promising anodes for high-rate potassium-ion batteries. J. Energy Chem. *53*, 155–162.

97. Lin, H., Li, M., Yang, X., Yu, D., Zeng, Y., Wang, C., et al. (2019). Nanosheets-Assembled CuSe Crystal Pillar as a Stable and High-Power Anode for Sodium-Ion and Potassium-Ion Batteries. Adv. Energy Mater. *9*, 1900323.

98. Xu, E., Li, P., Quan, J., Zhu, H., Wang, L., Chang, Y., et al. (2021). Dimensional Gradient Structure of $CoSe_2$@CNTs–MXene Anode Assisted by Ether for High-Capacity, Stable Sodium Storage. Nano-Micro Lett. *13*, 40.

99. Ge, J., Fan, L., Wang, J., Zhang, Q., Liu, Z., Zhang, E., et al. (2018). $MoSe_2$/N-Doped Carbon as Anodes for Potassium-Ion Batteries. Adv. Energy Mater. *8*, 1801477.

100. Zhang, L., Gu, X., Mao, X., Wen, S., Dai, P., Li, L., et al. (2021). Boosting fast and stable potassium storage of iron selenide/carbon nanocomposites by electrolyte salt and solvent chemistry. J. Power Sources *486*, 229373.

101. Yuan, S., Zhu, Y.H., Li, W., Wang, S., Xu, D., Li, L., et al. (2017). Surfactant-Free Aqueous Synthesis of Pure Single-Crystalline SnSe Nanosheet Clusters as Anode for High Energy- and Power-Density Sodium-Ion Batteries. Adv. Mater. *29*, 1602469.

102. Tan, H., Feng, Y., Rui, X., Yu, Y., and Huang, S. (2020). Metal Chalcogenides: Paving the Way for High-Performance Sodium/Potassium-Ion Batteries. Small Methods *4*, 2070002.

103. Chen, B., Chao, D., Liu, E., Jaroniec, M., Zhao, N., and Qiao, S.-Z. (2020). Transition metal dichalcogenides for alkali metal ion batteries: engineering strategies at the atomic level. Energy Environ. Sci. *13*, 1096–1131.

104. Luo, M., Yu, H., Hu, F., Liu, T., Cheng, X., Zheng, R., et al. (2020). Metal selenides for high performance sodium ion batteries. Chem. Eng. J. *380*, 122557.

105. Li, J., Hu, H., Qin, F., Zhang, P., Zou, L., Wang, H., Zhang, K., and Lai, Y. (2017). Flower-like $MoSe_2$ /C Composite with Expanded (0 0 2) Planes of Few-layer $MoSe_2$ as the Anode for High-Performance Sodium-Ion Batteries. Chemistry *23*, 14004–14010.

106. Liu, H., Guo, H., Liu, B., Liang, M., Lv, Z., Adair, K.R., et al. (2018). Few-Layer $MoSe_2$ Nanosheets with Expanded (002) Planes Confined in Hollow Carbon Nanospheres for Ultrahigh-Performance Na-Ion Batteries. Adv. Funct. Mater. *28*, 1707480.

107. Mahmood, A., Ali, Z., Tabassum, H., Akram, A., Aftab, W., Ali, R., Khan, M.W., Loomba, S., Alluqmani, A., Adil Riaz, M., et al. (2020). Carbon Fibers Embedded With Iron Selenide (Fe $_3$ Se $_4$) as Anode for High-Performance Sodium and Potassium Ion Batteries. Front Chem. *8*, 408.

108. He, Y., Wang, L., Dong, C., Li, C., Ding, X., Qian, Y., et al. (2019). In-situ rooting ZnSe/N-doped hollow carbon architectures as high-rate and long-life anode materials for half/full sodium-ion and potassium-ion batteries. Energy Storage Mater. *23*, 35–45.

109. Ma, M., Zhang, S., Yao, Y., Wang, H., Huang, H., Xu, R., et al. (2020). Heterostructures of 2D Molybdenum Dichalcogenide on 2D Nitrogen-Doped Carbon: Superior Potassium-Ion Storage and Insight into Potassium Storage Mechanism. Adv. Mater. *32*, 2000958.

110. Ou, X., Liang, X., Zheng, F., Wu, P., Pan, Q., Xiong, X., et al. (2017). In situ X-ray diffraction investigation of $CoSe_2$ anode for Na-ion storage: Effect of cut-off voltage on cycling stability. Electrochim. Acta *258*, 1387–1396.

111. Chen, K.-T., Chong, S., Yuan, L., Yang, Y.-C., and Tuan, H.-Y. (2021). Conversion-alloying dual mechanism anode: Nitrogen-doped carbon-coated Bi_2Se_3 wrapped with graphene for superior potassium-ion storage. Energy Storage Mater. *39*, 239–249.

112. Men, S., Zheng, H., Ma, D., Huang, X., and Kang, X. (2021). Unraveling the stabilization mechanism of solid electrolyte interface on ZnSe by rGO in sodium ion battery. J. Energy Chem. *54*, 124–130.

113. Zhang, Y., Tao, L., Xie, C., Wang, D., Zou, Y., Chen, R., et al. (2020). Defect Engineering on Electrode Materials for Rechargeable Batteries. Adv. Mater. *32*, 1905923.

114. Yin, Y., Zhang, Y., Gao, T., Yao, T., Zhang, X., Han, J., et al. (2017). Synergistic Phase and Disorder Engineering in 1T-$MoSe_2$ Nanosheets for Enhanced Hydrogen-Evolution Reaction. Adv. Mater. *29*, 1700311.

115. Zhang, S., Ai, Y., Wu, S.-C., Liao, H.-J., Su, T.-Y., Chen, J.-H., Wang, C.-H., Lee, L., Chen, Y.-Z., Xu, B., et al. (2019). 3D $CoMoSe_4$ Nanosheet Arrays Converted Directly from Hydrothermally Processed $CoMoO_4$ Nanosheet Arrays by Plasma-Assisted Selenization Process Toward Excellent Anode Material in Sodium-Ion Battery. Nanoscale Res. Lett. *14*, 213.

116. Luo, L., Song, J., Song, L., Zhang, H., Bi, Y., Liu, L., et al. (2019). Flexible Conductive Anodes Based on 3D Hierarchical Sn/NS-CNFs@rGO Network for Sodium-Ion Batteries. Nano-Micro Lett. *11*, 63.

117. Jia, X.-X., Yu, X.-Z., and Lu, B.-A. (2021). $Fe_{0.8}CoSe_2$ nanosphere coated by N-doped carbon for ultra-high rate potassium selenium battery. Rare Met. *40*, 2455–2463.

118. Sun, Z., Wu, X.L., Xu, J., Qu, D., Zhao, B., Gu, Z., et al. (2020). Construction of Bimetallic Selenides Encapsulated in Nitrogen/Sulfur Co-Doped Hollow Carbon Nanospheres for High-Performance Sodium/Potassium-Ion Half/Full Batteries. Small *16*, 1907670.

119. Peng, Q., Ling, F., Yang, H., Duan, P., Xu, R., Wang, Q., et al. (2021). Boosting potassium storage performance via construction of $NbSe_2$–based misfit layered chalcogenides. Energy Storage Mater. *39*, 265–270.

120. Ma, F., Lu, J., Pu, L., Wang, W., and Dai, Y. (2020). Construction of hierarchical cobalt-molybdenum selenide hollow nanospheres architectures for high performance battery-supercapacitor hybrid devices. J. Colloid Interface Sci. *563*, 435–446.

121. Wan, Y., Song, K., Chen, W., Qin, C., Zhang, X., Zhang, J., et al. (2021). Ultra-High Initial Coulombic Efficiency Induced by Interface Engineering Enables Rapid, Stable Sodium Storage. Angew. Chem. Int. Ed. *60*, 11481–11486.

122. Cheng, N., Zhao, J., Fan, L., Liu, Z., Chen, S., Ding, H., Yu, X., Liu, Z., and Lu, B. (2019). Sb-MOFs derived Sb nanoparticles@porous carbon for high performance potassium-ion batteries anode. Chem. Commun. (Camb.) *55*, 12511–12514.

123. Wang, H., Yu, D., Wang, X., Niu, Z., Chen, M., Cheng, L., et al. (2019). Electrolyte Chemistry Enables Simultaneous Stabilization of Potassium Metal and Alloying Anode for Potassium-Ion Batteries. Angew. Chem. Int. Ed. *58*, 16451–16455.

124. Tian, Y., An, Y., Xiong, S., Feng, J., and Qian, Y. (2019). A general method for constructing robust, flexible and freestanding MXene@metal anodes for high-performance potassium-ion batteries. J. Mater. Chem. A Mater. Energy Sustain. *7*, 9716–9725.

125. Liu, S., Mao, J., Zhang, L., Pang, W.K., Du, A., and Guo, Z. (2021). Manipulating the Solvation Structure of Nonflammable Electrolyte and Interface to Enable Unprecedented Stability of Graphite Anodes beyond 2 Years for Safe Potassium-Ion Batteries. Adv. Mater. *33*, 2006313.

126. Deng, L., Zhang, Y., Wang, R., Feng, M., Niu, X., Tan, L., and Zhu, Y. (2019). Influence of KPF_6 and KFSI on the Performance of Anode Materials for Potassium-Ion Batteries: A Case Study of MoS_2. ACS Appl. Mater. Interfaces *11*, 22449–22456.

127. Fiore, M., Wheeler, S., Hurlbutt, K., Capone, I., Fawdon, J., Ruffo, R., et al. (2020). Paving the Way toward Highly Efficient, High-Energy Potassium-Ion Batteries with Ionic Liquid Electrolytes. Chem. Mater. *32*, 7653–7661.

128. Onuma, H., Kubota, K., Muratsubaki, S., Hosaka, T., Tatara, R., Yamamoto, T., et al. (2020). Application of Ionic Liquid as K-Ion Electrolyte of Graphite//$K_2Mn[Fe(CN)_6]$ Cell. ACS Energy Lett. *5*, 2849–2857.

129. Placke, T., Kloepsch, R., Dühnen, S., and Winter, M. (2017). Lithium ion, lithium metal, and alternative rechargeable battery technologies: the odyssey for high energy density. J. Solid State Electrochem. *21*, 1939–1964.

130. Xiao, Z., Meng, J., Xia, F., Wu, J., Liu, F., Zhang, X., et al. (2020). K^+ modulated K^+/vacancy disordered layered oxide for high-rate and high-capacity potassium-ion batteries. Energy Environ. Sci. *13*, 3129–3137.

131. Shah, A., Ates, M.N., Kotz, S., Seo, J., Abraham, K., Somu, S., et al. (2014). A Layered Carbon Nanotube Architecture for High Power Lithium Ion Batteries. J. Electrochem. Soc. *161*, A989.